Mapping Nanoscale Metal-Insulator Phase Transition in $NdNiO_3$ and Molecular Beam Epitaxy of $SmTiO_3$ Thin Films

A thesis submitted to the
College of Graduate and Postdoctoral Studies
in partial fulfillment of the requirements
for the degree of Master of Science
in the Department of Physics and Engineering Physics
University of Saskatchewan
Saskatoon

By
Jessica A. Freese

Permission to Use

In presenting this thesis in partial fulfillment of the requirements for a Postgraduate degree from the University of Saskatchewan, I agree that the Libraries of this University may make it freely available for inspection. I further agree that permission for copying of this thesis in any manner, in whole or in part, for scholarly purposes may be granted by the professor or professors who supervised my thesis work or, in their absence, by the Head of the Department or the Dean of the College in which my thesis work was done. It is understood that any copying or publication or use of this thesis or parts thereof for financial gain shall not be allowed without my written permission. It is also understood that due recognition shall be given to me and to the University of Saskatchewan in any scholarly use which may be made of any material in my thesis.

Disclaimer

Reference in this thesis to any specific commercial products, process, or service by trade name, trademark, manufacturer, or otherwise, does not constitute or imply its endorsement, recommendation, or favoring by the University of Saskatchewan. The views and opinions of the author expressed herein do not state or reflect those of the University of Saskatchewan, and shall not be used for advertising or product endorsement purposes.

Requests for permission to copy or to make other uses of materials in this thesis in whole or part should be addressed to:

Head of the Department of Physics and Engineering Physics
163 Physics Building
116 Science Place
University of Saskatchewan
Saskatoon, Saskatchewan
Canada
S7N 5E2

OR

Dean

College of Graduate and Postdoctoral Studies

University of Saskatchewan

116 Thorvaldson Building, 110 Science Place

Saskatoon, Saskatchewan S7N 5C9 Canada

Abstract

The subject of this thesis is the growth and characterization of quantum materials. Quantum materials are those in which correlated electron interactions result in functional emergent properties like high-temperature superconductivity, colossal magnetoresistance, ferromagnetism, and metal-insulator transitions. 3d transition metal oxides, particularly perovskites, have been found to be a fertile area of investigation in quantum materials. Rare earth nickelates and titanates fall into this category and are examined here. The bulk of this work concerns soft x-ray spectroscopy and imaging of a free-standing $NdNiO_3$ thin film. $NdNiO_3$ displays a metal-insulator transition as well as a magnetic transition, with the respective Curie and Néel temperatures coinciding.

We employ x-ray absorption spectroscopy to characterize the electronic transition from metallic to insulating on cooling the sample, noting the magnitude of the hysteresis in the process; x-ray magnetic scattering to characterize the magnetic transition on heating; and scanning transmission x-ray spectromicroscopy to search for the formation of distinct domains of metallic and insulating phases during the progress of the electronic phase transition. Although these electronic domains were not observed, the sum of our experiments present confirmation that freestanding films of this novel configuration possess similar magnetic and electronic properties to those observed in their bulk counterparts. This finding is significant as it indicates that films of this type could be integrated into device applications in the same manner as bulk nickelates.

A secondary thrust of this work is the development of the capability to synthesize thin films by molecular beam epitaxy (MBE) at the Canadian Light Source for future studies of quantum materials with an emphasis on interface effects and heterostructures. We briefly present results of an effort to grow $SmTiO_3$ thin films by MBE with characterization by electron diffraction and spectroscopy.

Acknowledgements

I would like to thank my advisor, Prof. Robert Green, for his patience, support, and guidance; Dr. Fengmiao Li and Dr. Ronny Sutarto for their generosity with their time and expertise; the members of my advisory committee, Prof. Alex Moewes, Prof. Kathryn Williams, and Prof. Kaori Tanaka for their helpful guidance and feedback; and my fellow lab group members Patrick Braun, Niyusha Hosseini, and Skylar Koroluk for many helpful conversations and companionship during odd hours at the beamline.

I would also like to thank our collaborators at University of Antwerp and University of Twente for the provision of samples and STEM data. This work was made possible by funding from NSERC.

Contents

List of Tables

List of Figures

List of Abbreviations

CLS	Canadian Light Sources
EELS	Electron Energy Loss Spectroscopy
EPU	Elliptically Polarizing Undulator
HAADF	High-Angle Annular Dark-Field
ID	Insertion Device
LB	Langmuir-Blodgett
MBE	Molecular Beam Epitaxy
MIT	Metal-Insulator Transition
PCA	Principal Component Analysis
PLD	Pulsed Laser Deposition
PMT	Photomultiplier Tube
REIXS	Resonant Elastic and Inelastic Scattering (CLS Beamline, 10ID-2)
RF	Radio Frequency
RHEED	Reflection High Energy Electron Diffraction
SM	Spectromicroscopy (CLS Beamline, 10ID-1)
STEM	Scanning Transmission Electron Microscopy
STXM	Scanning Transmission X-ray Microscopy
SVD	Singular Value Decomposition
TEM	Transmission Electron Microscopy
TEY	Total Electron Yield
XAS	X-ray Absorption Spectroscopy
X-PEEM	X-ray Photoemission Electron Microscopy
XPS	X-ray Photoelectron Spectroscopy
XRD	X-ray Diffraction

1 INTRODUCTION

In 1965, in an article romantically entitled "Cramming more components onto integrated circuits", Intel co-founder Gordon Moore expressed a vision of an astonishing future: "Integrated circuits will lead to such wonders as home computers-or at least terminals connected to a central computer [...]", he marveled [1]. He had observed a trend that approximately every year, the complexity of integrated circuits doubled—every year twice as many transistors would fit on the same microchip, and predicted that this rapid advancement would continue until 1975. When his prediction was borne out, he made another impressively accurate prediction which has since become known as Moore's law: the number of transistors on a microchip doubles approximately every two years while the production cost halves. This trend is illustrated in Figure 1.1. This incredible rate of growth has persisted and enabled the technologies on which our modern world depends.

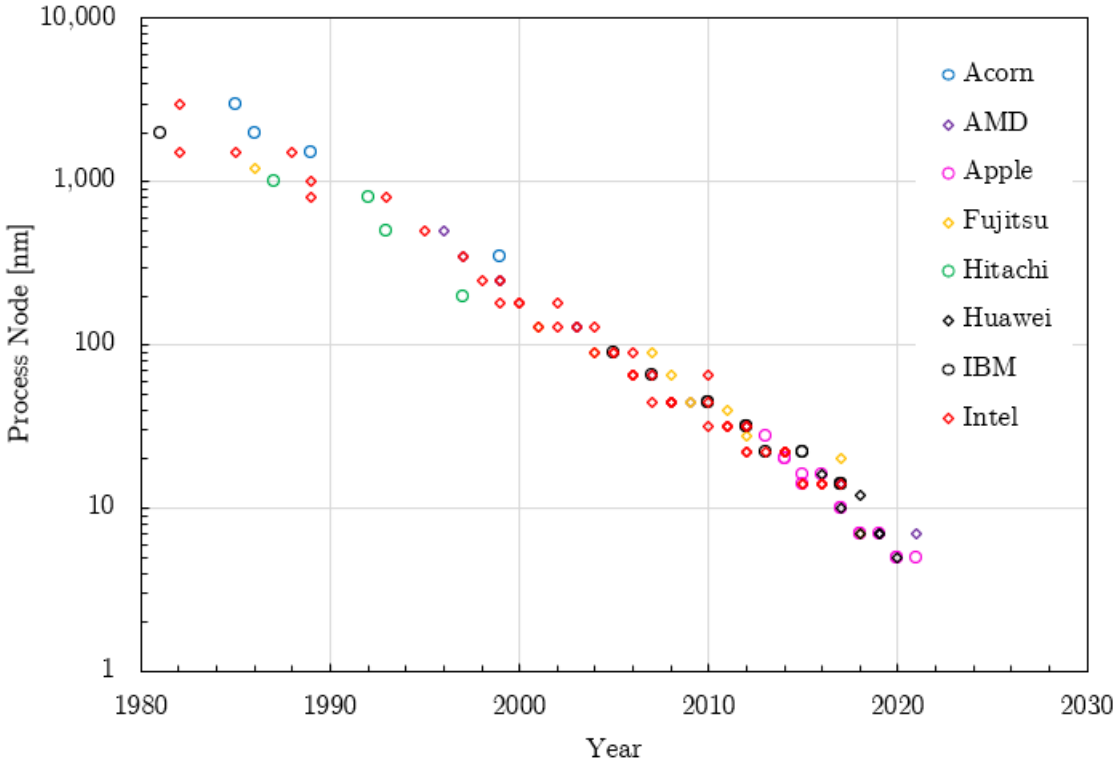

Figure 1.1: For many years, the semiconductor industry has used "Process Nodes" as a metric for their advances. This was originally a simple measure of the transistor gate length, but in recent years the process nodes have ceased to directly correlate to a physical feature size [2]. Device performance has continued to improve, but this owes less to the transistor gate length and more to new transistor architectures than is implied by the process nodes. All plotted semiconductor process data from online CPU archives [3–6].

Now we are nearing the point at which the rapacious growth predicted by Moore's law can no longer be sustained by simply reducing the size of conventional semiconductor electronics—as the resolution of fabrication methods has dramatically improved, our constraints are less of manufacturability than of the fundamental properties of the materials themselves. Development of materials with novel electronic and magnetic properties is essential to enable the technologies of tomorrow. Fortunately, we have some idea of where to look.

1.1 Quantum Materials

The properties of the materials which have been crucial to the semiconductor industry and the modern computing world have been well described by quantum theory from the early 20th century. These materials typically have delocalized electrons which can be treated en masse—a "sea" of electrons in an ionic lattice. The electronic band structure can then be calculated from the imposed boundary conditions.

Over the years, exceptions have cropped up—materials whose properties are not predicted by this treatment. One classic example is NiO, which has a nearly full 3d shell and is predicted by this theory to be a conductor, but due to electron interactions it actually has an insulating electronic structure. NiO is an example of a correlated electron material, and more specifically a Mott insulator. There exist many other materials in which correlated electron interactions result in unusual properties. The term "quantum materials" has been assigned to materials wherein correlated electron interactions give rise to functional emergent properties like high-temperature superconductivity, colossal magnetoresistance, ferromagnetism, and metal-insulator transitions. Since the discovery of high temperature superconductivity in doped cuprates in 1986, there has been an enormous amount of research devoted to identifying and tuning novel properties and novel materials. This trend is illustrated in Figure 1.2, which shows the growth in yearly publications regarding quantum materials and correlated electron systems.

In the search for new quantum materials, it has been found that transition metal oxides wherein the transition metal is in the 3+ or 4+ oxidation state are a fertile area to examine. In particular, we often look to the perovskites (ABO_3) and spinels (A_2BO_4) whose A site atoms are either rare earth metals or alkaline earth metals like calcium, strontium, and barium, and B site atoms are transition metals. The rare earth metals are most stable in the 3+ oxidation state and the alkaline earth metals are only stable in the 2+ oxidation state. With the oxygen atoms completing their 2p orbitals (O^{2-}), the B site transition metal atoms are forced into a higher oxidation state (3+ or 4+). Numerous perovskites and spinels, both

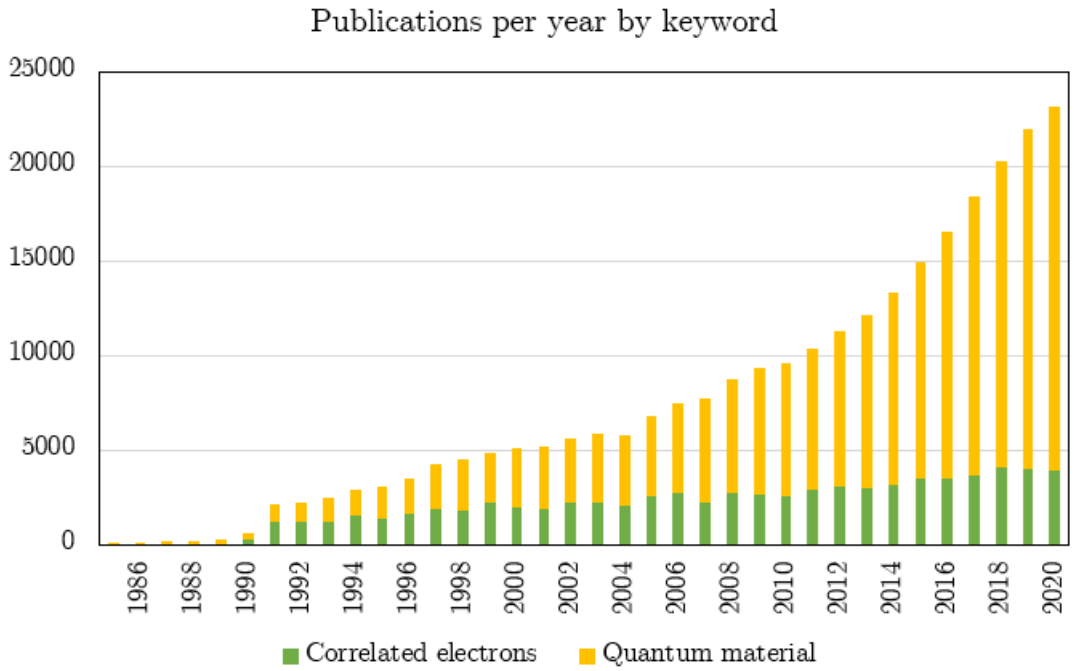

Figure 1.2: Publication trends in correlated electron systems and quantum materials starting from the first reports of cuprate superconductivity.

doped and undoped have been extensively studied and found to possess emergent properties, but there continue to be new discoveries in this set of crystalline materials. Additionally, new properties are being discovered in well characterized materials when strained and at interfaces, as achieved in heterostructure thin films. The nickelates ($RNiO_3$, where R indicates a rare earth element) are one such family. With the exception of $LaNiO_3$, the $RNiO_3$ compounds display a metal-insulator transition as well as a magnetic transition between paramagnetic and anti-ferromagnetic states. The temperatures at which these transitions occur scale with the ionic radius of the rare earth atom. Depending on the choice of rare earth metal, a magnetic phase transition may also be coincident; this is the case for R = Pr or Nd [7]. This trend is shown in Figure 1.3. The bulk of this thesis pertains to the examination of the nature of the metal-insulator transition in thin films of $NdNiO_3$.

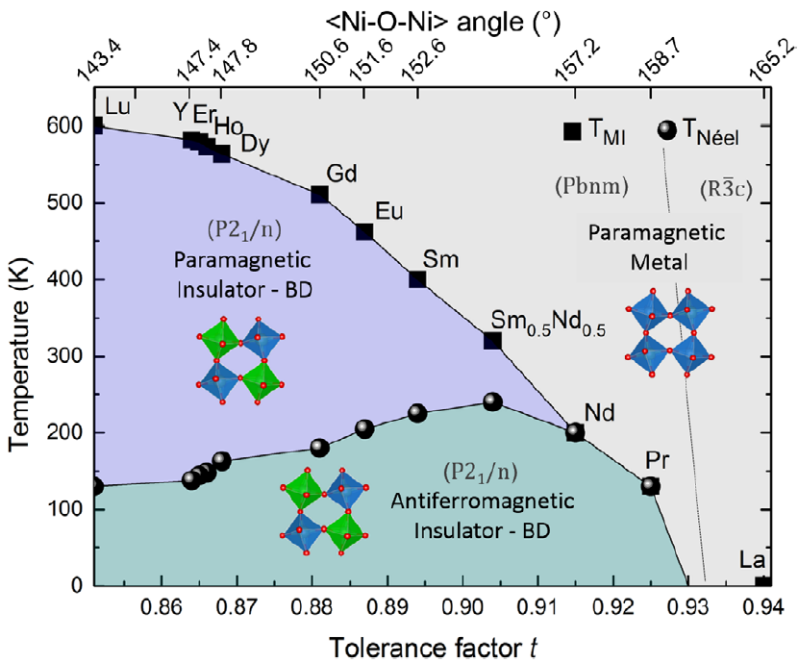

Figure 1.3: Phase diagram of nickelates with varying rare earth metals in the A site. Reproduced from figure 4 of Catalano et al (2018) Rep. Prog. Phys. **81** (4) 046501.

1.2 Project and Organization of this Thesis

In Chapter 2 we will cover the fundamental physics and characterization techniques relevant to two distinct experimental projects, both of which consist of the examination of transition metal oxide thin films possessing emergent properties. In Chapter 3, we will discuss the experimental details and results of the first of these: spectroscopy and imaging of a freestanding thin film of $NdNiO_3$. The fourth chapter will address the second experimental project: growth of $SmTiO_3$ thin films on traditional wafer substrates.

Previous studies have extensively characterized the resistivity properties of $NdNiO_3$ thin films and recent work using surface sensitive techniques has focused on localized electronic behaviour in thin films. In particular, it has been observed that distinct insulating and metallic domains nucleate as the metal-insulator transition progresses–a phenomenon known as nanoscale phase separation. These studies present results with some variation in range of transition temperatures, hysteresis magnitudes, and domain size and behaviour, but they

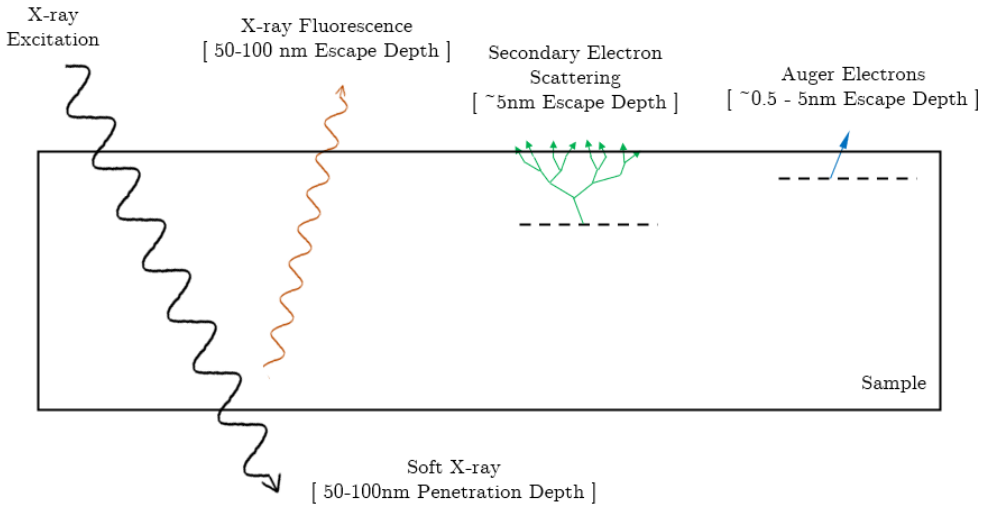

Figure 1.4: Approximate escape depths for possible signals from a sample excited by x-rays including Auger electrons, secondary electron scattering, x-ray fluorescence, and transmitted beams. After a figure by F. Nolting [11].

are united in their use of surface sensitive techniques–primarily x-ray photoemission electron microscopy (X-PEEM) [8] [9] [10]. X-PEEM relies on secondary electron emission for detection and is only sensitive to the top 5 nm of the sample as this is the escape depth of the electrons. A comparison of the depth sensitivity of several types of sample signals is shown in Figure 1.4. This bias towards surface sensitive techniques served as a strong motivation for us to apply a more penetrative technique to a similar sample. Collaborators at the University of Twente were able to provide a $NdNiO_3$ thin film grown on a nanosheet substrate supported by a TEM grid. To our knowledge, this is the first sample to be grown in this manner. This unusual sample configuration enabled us to use scanning transmission x-ray microscopy (STXM), a technique capable of probing the entirety of samples of thickness less than 50 - 100 nm. In this work, we present spectromicroscopy data for the bulk of a 50 nm thick $NdNiO_3$ film in order to test our hypothesis that the variance in the reported domain structures is due to surface effects and a more accurate view of domain formation can be achieved by probing greater depth.

We had also hoped to compare the results from this technique with those for a $SmNiO_3$ film. In $NdNiO_3$, the Néel temperature and metal-insulator transition temperature, T_{MI}

are concurrent, but in $SmNiO_3$, they are decoupled. Having data from these otherwise very similar systems would have been valuable in separating out the magnetic and electronic behaviours, but unfortunately, during the allotted beam time, we had technical problems and were unable to complete the data collection for this second thin film.

The second experimental section in this thesis describes a series of epitaxial growth runs aimed at determining and refining the growth parameters for thin films of $SmTiO_3$. The motivations for this growth effort are the reports of interesting phenomena in $SmTiO_3$ thin films and heterostructures. A carrier density dependent metal-insulator transition has been reported at the interface in $SmTiO_3$ films grown on $SrTiO_3$ and other work has concerned quantum critical behaviour in quantum wells in $SmTiO_3/SrTiO_3$ heterostructures [12] [13]. In this work, several $SmTiO_3$ thin films are grown by molecular beam epitaxy (MBE) and characterized in terms of morphology using reflection high energy electron diffraction (RHEED) and chemically using x-ray photoelectron spectroscopy (XPS).

2 BACKGROUND

As this thesis is primarily concerned with the use of synchrotron radiation to study correlated oxides, it is prudent to devote some time to background information pertaining to the properties of synchrotron radiation, x-ray characterization techniques, and materials science topics including correlated perovskite oxides and thin films more generally. In Section 2.1 we will cover how synchrotron radiation is generated as well as spectroscopy and imaging techniques which employ it. In Section 2.2 we will cover electronic and magnetic phase transitions in solids, some relevant crystal structures, and the basics of epitaxial thin film growth.

2.1 Synchrotron Radiation and Techniques

2.1.1 Generation of Synchrotron Radiation

The production of synchrotron radiation begins with an electron gun which produces a beam of electrons. The beam passes through a series of accelerating structures which use radio frequency (RF) standing waves to pass energy to the electrons. This portion is known as the linear accelerator or linac. Once the beam has reached the end of the linac, it enters the booster ring which contains bend magnets to keep the beam circulating and more RF cavities to accelerate the beam to the desired maximum energy. After the booster ring, the high energy beam is injected into the storage ring where it circulates on a tightly controlled orbit regulated by magnetic structures [14]. Dipole magnets are used to turn the beam, quadrupole magnets focus the beam, and sextupole magnets allow for correction of chromatic aberrations. A simplified layout of the basic elements of a synchrotron is shown in Figure 2.1. Whenever the beam turns, it produces synchrotron radiation. Passing through a dipole magnet structure produces a wide fan of x-rays in the plane of the bend which is

highly collimated in the direction normal to the plane. The energy of this fan is broadband and the peak energy is determined by the energy of the electron beam and the bend radius of the dipole magnet.

In early synchrotrons, bend magnets were the only source of radiation used by beamlines. Further development work resulted in insertion devices using a series of periodically arranged opposing dipole magnets to fine tune the radiation generated. The first of these devices is the wiggler which produces radiation with a broad energy range, but of higher intensity than that from a bend magnet. The second is the undulator which uses magnetic structures with smaller periods, thus reducing the beam deflection and keeping the radiation fans tightly focused rather than diverging. This also causes an interference pattern which results in high intensity quasi-monochromatic radiation. The energy of this radiation can be tuned by adjusting the gap between the magnet poles to change the magnetic field strength. An example of the spectra produced by these three types of insertion devices is shown in Figure 2.2. The beamlines used (SM and REIXS at the CLS) in the present work use radiation from an elliptically polarizing undulator (EPU) which enables the delivery of an x-ray beam of not only tunable energy, but of polarization arbitrarily controlled by the user. This is achieved by applying a small lateral offset to the periodic structure.

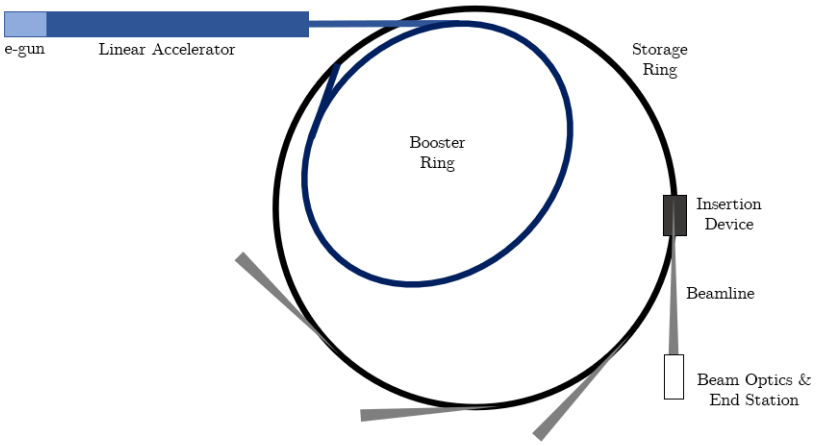

Figure 2.1: Schematic of the basic elements of a synchrotron including the linear accelerator, booster ring, storage ring, and insertion devices leading to beamlines.

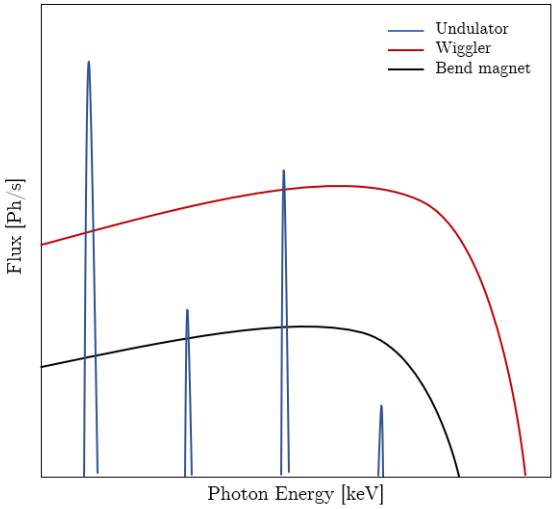

Figure 2.2: Typical radiation produced by a bend magnet, wiggler, and undulator.

Once the radiation has been produced by the insertion device, a series of dedicated x-ray optics are used to steer the beam, achieve the desired level of focus, and select the beam energy as needed. Typical beamline optics include slits, mirrors, monochromators, and zone plates. Entrance and exit slits narrow and collimate by excluding portions of the incoming x-ray beam. Depending on the curvature, coating, and angle of incidence, mirrors can be used for focusing, harmonic rejection, and power modulation. Monochromators employ diffraction to filter out undesired wavelengths and require a highly collimated input in order to be effective. For most soft x-rays (photon energies from 120 eV to 5000 eV), a diffraction grating can be used, but for shorter wavelengths (hard x-rays) it is necessary to use high quality single crystals [15]. Radiation which does not meet the Bragg diffraction condition for the given geometry is excluded. Curved monochromators can simultaneously provide beam focusing, but are less suited to cases where the beam energy may be tuned rather than fixed. Another diffractive x-ray optic is the Fresnel zone plate which is a transmissive diffraction grating employing concentric circles to achieve an effect much like a traditional lens for visible light. Radiation of different energies will have a different focal length, thus zone plates can improve the monochromaticity of the incoming beam as well as produce focusing suitable for high resolution scanning microscopies [14].

For the STXM end station at the SM beamline, the optical path begins with a cylin-

drical mirror to achieve high vertical collimation prior to the plane grating monochromator (PGM). The PGM has three gratings with varying line spacing to accommodate different energy regimes from 130 eV up to 2500 eV. The monochromated beam is then focused with a toroidally curved mirror which provides focusing in the vertical and horizontal directions. The last optical element is a Fresnel zone plate which focuses the beam onto the sample, achieving a spot size of 30 nm, energy resolution (ΔE/E) of 1 x 10^{-4} at 800 eV, and photon flux of 1x10^{8} photons/second. [16] [17].

The REIXS beamline is fed by an EPU identical to that used by the SM beamline and thus has a similar range of accessible beam energies, but achieves distinctly different spot size and energy resolution with a different set of optics. The Resonant Soft X-ray Scattering (RSXS) end station at REIXS uses a cylindrical mirror for initial collimation before a variable line spacing plane grating monochromator (VLS-PGM) with several different gratings and coatings available. The remaining focusing is achieved with a an elliptical mirror and another cylindrical mirror. The spot size at the sample is 250 µm x 150 µm with an energy resolution (ΔE/E) of 1.3 x 10^{-4} at 1 keV, and photon flux of 5x10^{11} photons/second at 1 keV.

2.1.2 Advantages of Synchrotron Radiation

Synchrotron sources present a remarkable enhancement to some common x-ray based techniques and enable others which would otherwise be both impractical and horrendously expensive. Most lab instruments employing x-rays rely on the same generation mechanism: inside of a vacuum tube a biased filament is heated, and the emitted electrons are accelerated to strike a metal anode composed of an element chosen for its particular characteristic x-ray emission lines. The anode will emit these lines as well as a weak broad spectrum of x-rays known as bremsstrahlung or "braking radiation". These x-rays then pass through at least one monochromator to produce a focused and monochromatic beam which can be used for x-ray diffraction (XRD) or as an excitation source for x-ray photoelectron spectroscopy (XPS).

For XRD, most instruments use a copper anode and select for the K_α emission line at

$\lambda = 1.54056$ Å. Being restricted to this wavelength imposes a limit on the crystal planes which can be measured. The relatively low photon flux from an x-ray tube can also present problems when measuring higher order planes which tend to have lower scattered intensities. For XPS, the wavelength restriction is not a significant problem, but higher flux is always desirable.

While XRD and XPS can be enhanced by using synchrotron radiation, x-ray absorption spectroscopy (XAS) is impossible without it. XAS relies on tunable x-ray energy which is not achievable using an anode based x-ray source. Further, the tuning range of the source determines the elements which can be examined, so a narrow tuning range presents a serious limitation to the utility of this technique.

2.1.3 X-ray Absorption Spectroscopy

XAS is a spectroscopy technique wherein an incident monochromatic beam of x-rays strikes the sample and some portion of the beam is absorbed. The absorption can be measured by detecting sample fluorescence, emitted photoelectrons, and in the case of very thin samples the remaining transmitted beam. The x-ray energy is tuned across the spectral range of interest, typically including one or more absorption edges corresponding to ejected core electrons. A K-edge absorption corresponds to the ejection of a 1s core electron. L_2 and L_3 edges correspond to the ejection of 2p core electrons, but are distinct from one another due to spin orbit splitting as shown in Figure 2.3. As the beam energy approaches the edge, absorptions correspond to transitions to bound states, shedding light on oxidation state, ligand type, and coordination geometry [18] [19] [20]. For transition metals, $L_{2,3}$ edge excitations into 3d orbitals tend to dominate the spectra and yield a great deal of information. Different elements can be distinguished by the differing characteristic absorption edge energies. The spectral shape is sensitive to the d electron count and the local bonding environment, thus allowing us to discern oxidation state as well as coordination [21].

In this work we will concern ourselves solely with the Ni $L_{2,3}$ XAS, using changes in peak shape to distinguish between metallic and insulating states in $NdNiO_3$ thin films [22].

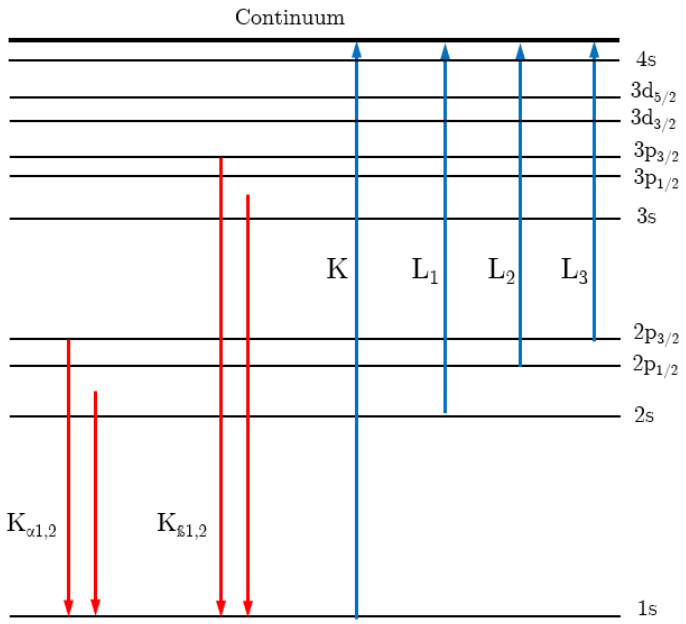

Figure 2.3: Atomic energy levels for a 3d transition metal. X-ray emission lines are shown in red, while x-ray absorption transitions are shown in blue.

2.1.4 Scanning Transmission X-ray Spectromicroscopy

Scanning Transmission X-ray Spectromicroscopy (STXM) is a rastered imaging technique which relies on XAS. In a STXM apparatus the incident x-ray beam is focused onto the sample and the transmitted beam is detected, thus the sample must be thin enough for use in a transmission geometry [16] [17]. As in XAS, the incident x-ray energy is tuned across an absorption edge while recording the transmitted intensity. The key difference is that instead of a single detector value or several channels to be averaged at each energy, the output of STXM is an image wherein each pixel has an associated XAS spectrum. The set of these images across the target spectral region is called a stack. A typical STXM stack and associated XAS spectra are illustrated in Figure 2.4. Some sample movement can be accounted for in post-processing, but for good results, the sample and sample holder must be well stabilized against vibrations and temperature fluctuations.

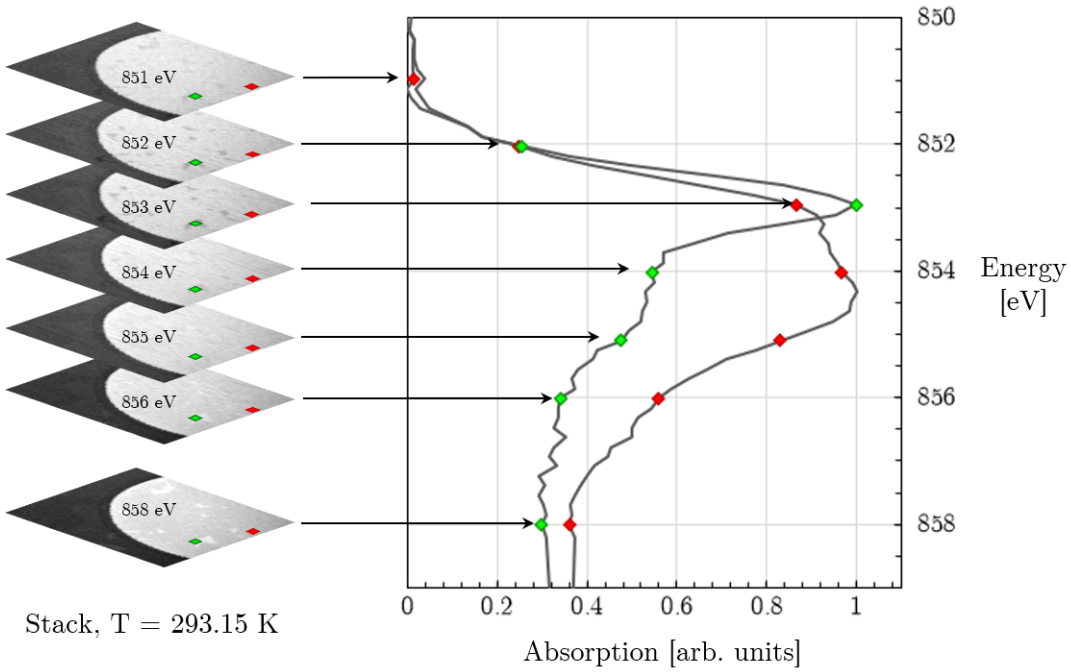

Figure 2.4: Visualization of how XAS spectra can be extracted from a typical STXM stack. Shown at the left is a truncated stack (7 images selected from a stack containing more than 50). Each stack image is labelled with the approximate x-ray energy during image acquisition. Two sample regions chosen for spectra extraction are indicated by red and green diamonds. Shown at the right are the XAS spectra from these regions.

2.2 Relevant Solid State Considerations

In this work we are principally concerned with identifying two phases of a particular perovskite nickelate and characterizing the transition between them as it occurs, so it stands to reason that we must begin by defining what we mean by phases.

2.2.1 Phase Transitions

The term "phase" is frequently casually used as a synonym for "state of matter", the list of which, outside of extreme temperature and pressure conditions, comprises solid, liquid, gas, and plasma, but phases lend a greater level of specificity. A phase is a collection of matter for which the chemical and physical properties are uniform. In the solid state different crystal structures or amorphous forms of a given compound would be considered distinct phases. Phase transitions occur when temperature and/or pressure conditions change such that the matter in question changes from one phase to another. The conditions under which a given phase is stable and where transitions occur are most commonly conveyed by phase diagrams like the one shown in Figure 2.5.

The most obvious examples of phase transitions are those from one state of matter to another: melting, freezing, evaporating, and subliming, but there are many more subtle transitions. A central concern of bulk solution crystal growth is that small deviations from the optimum temperature and solution saturation conditions to grow a particular phase can result in an undesired phase nucleating and converting the entire boule.

A ferromagnetic material heated above a particular temperature known as the Curie point will become paramagnetic, i.e. the spin ordering which allowed a bulk magnetic field to exist at the low temperature is disrupted and the disordered spins cancel one another out in the absence of an applied magnetic field. Analogously, an antiferromagnetic material will become paramagnetic when heated above its Néel temperature. Other magnetic ordering transitions are also possible.

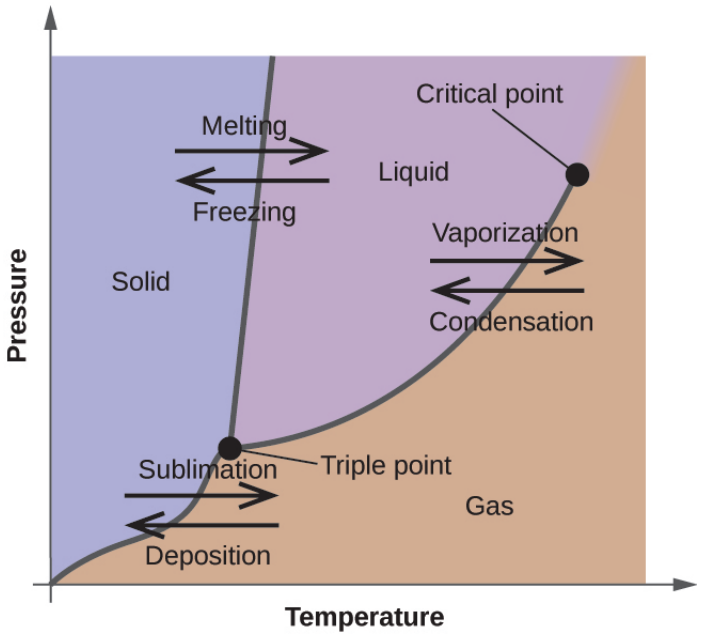

Figure 2.5: Basic phase diagram showing solid, liquid, and gas phases as well as the transitions between phases. Reproduced from [23].

In addition to magnetic phase transitions there are electronic ones. These may be influenced by structural factors or other considerations. Superconductors fall into this category as do materials which display a metal-insulator transition. Metal-insulator transitions are characterized by a change in resistance of several orders of magnitude.

In the Landau theory of phase transitions, transitions are characterized by an order parameter specific to the system which represents the free energy of the system at and near the critical point. In this framework a distinction is drawn between abrupt, discontinuous phase transitions and gradual, continuous ones. In the former case, "first order",the first derivative of the free energy function is discontinuous and in the latter, "second order", the second derivative of the free energy function is discontinuous. Hysteresis behaviour is indicative of a first order phase transition—some energy is either released or absorbed when the system transitions from some phase A to another phase B, and vice versa, resulting in a different critical temperature when heating and cooling [10] [24]. Hysteresis is a phenomenon most widely known as a characteristic of ferromagnetic and ferroelectric materials in changing applied magnetic and electric fields respectively. In the case of ferromagnetics, as the applied

field increases the magnetic moments align with the field until reaching a saturation point. If the applied field is reduced or eventually reversed in polarity, the magnetic moments begin to realign in reverse, but this process is asymmetric. The shape of the curve is dependent on the initial state: the order or lack of order at the outset is influential. Hysteresis is also present in metal-insulator transitions where we see a similar difference in the conductivity of the material as it is heated or cooled through the transition temperature range.

2.2.2 Crystal Structure

The primary crystalline material examined in this work is $NdNiO_3$ which is a perovskite, however some defects observed in the sample are structurally different, so it is worthwhile to briefly describe the relevant structures.

Perovskite oxides have a chemical formula of ABO_3 where the A-site cation is an alkaline earth or rare-earth metal and the B-site cation is a transition metal. As illustrated in Figure 2.6, an ideal cubic perovskite unit cell, the B-site atom is body-centred at ($\frac{1}{2}$, $\frac{1}{2}$, $\frac{1}{2}$) and surrounded by face-centred oxygen atoms. The A-site atoms are located at the corners of the unit cell. Depending on the ionic radii of the cations, the structure may be distorted from the ideal cubic [25]. Rare-earth nickelates, of the form $RNiO_3$ are orthorhombically distorted at room temperature and at low temperature undergo a structural phase transition to a monoclinic unit cell [26].

In $NdNiO_3$, we expect the neodymium to be in its most stable oxidation state (Nd^{3+}) and the oxygen to completely fill its 2p orbital, thus leaving it in the 2- oxidation state. With these conditions, for the compound to be charge neutral the nickel must be in the 3+ oxidation state. Recent work has shown that this is not strictly accurate and that the nickel ground state is actually [Ar] $3d^8$ $\underline{L}$ where the $\underline{L}$ indicates a ligand hole in the oxygen 2p orbital [27] [22]. Nonetheless, it continues to be useful when discussing the spectroscopic character of this compound to describe it as formally Ni^{3+}.

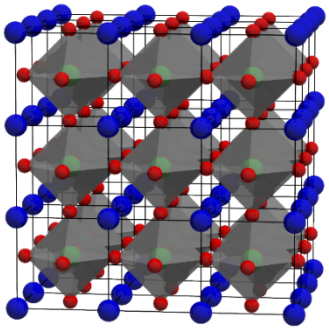

Figure 2.6: Ideal cubic perovskite lattice with A-site cations shown in blue, B-site in green, and oxygen atoms in red. The BO_6 octahedra are shown in gray. Figure used with permission from creator, Robert Green.

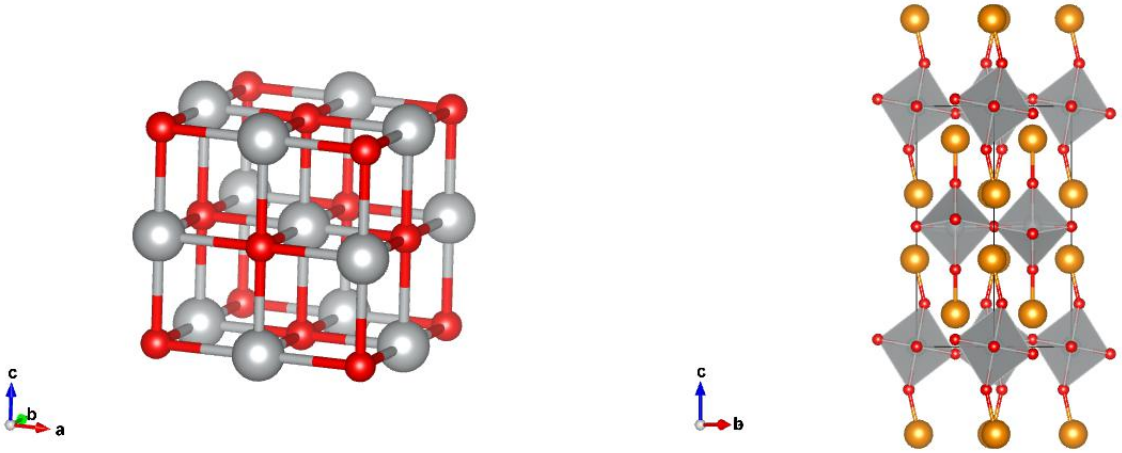

Figure 2.7: Left, rock-salt cubic structure. Right, RP phase, a layered perovskite with n-repeating layers.

Potential defect structures found in $NdNiO_3$ are NiO and Nd_2NiO_4 which are structurally rock-salt cubic and Ruddlesden-Popper (RP) phase respectively. These two structures are shown in Figure 2.7. The rock-salt structure is composed of two interpenetrating face-centered cubic lattices of the two constituent atoms. The RP phase could be considered a hybrid between rock-salt and perovskite in which the two are layered. In both of these cases, we have Ni^{2+}.

Setting aside the question of defects, it is useful to spend some time on the matter of lattice mismatch and strain in thin films. In epitaxial growth the crystallographic orientation of the film grown is influenced by the orientation and lattice parameters of the substrate

crystal–the new growth mimics the scaffold. Aside from the case of homoepitaxy, wherein the grown film is the same as the substrate, there will almost always be some level of mismatch between the substrate and the film. If this mismatch is large enough (typically 15% or higher), the growth will be unsuccessful [28]. In cases where the growth is successful, the lattice mismatch may still be significant and cause epitaxial layers (epilayers) to form defects or to distort to more closely match the in-plane lattice constants of the substrate. This type of distortion results in a strain energy which can influence the electronic structure. As shown in Figure 2.8, the metal insulator transition behaviour in $NdNiO_3$ thin films is different for epitaxial substrates of varying lattice parameters. A comparison of the lattice parameters of these materials as well as the CNO nanosheet substrate used in this work is shown in Table 2.1.

Calculations for strain energy in an epitaxial film tend to assume that the substrate can be treated as infinite—that it is dramatically thicker than the epitaxial film and any strain energy is stored in the deposited material [29]. Since our film substrate is a nanosheet, obviously this is not a valid assumption. Although CNO has a similar lattice mismatch to other commonly used substrates for $NdNiO_3$ growth, the $NdNiO_3$ lattice may not store as much of the strain energy.

Table 2.1: Lattice parameters of $NdNiO_3$ and selected epitaxial growth substrates [7] [30].

	a_{pc}	a [Å]	b [Å]	c [Å]	Lattice Mismatch (NNO)
$NdNiO_3$ (NNO)	3.807	5.3891	5.3816	7.6101	0%
$LaAlO_3$ (LAO)	3.789	5.365	5.365	13.111	0.48%
$NdGaO_3$ (NGO)	3.858	5.428	5.498	7.709	-1.32%
$SrTiO_3$ (STO)	3.905	3.905	3.905	3.905	-2.51%
$Ca_2Nb_3O_{10}$ (CNO)	3.86	3.86	3.86	-	-1.37%

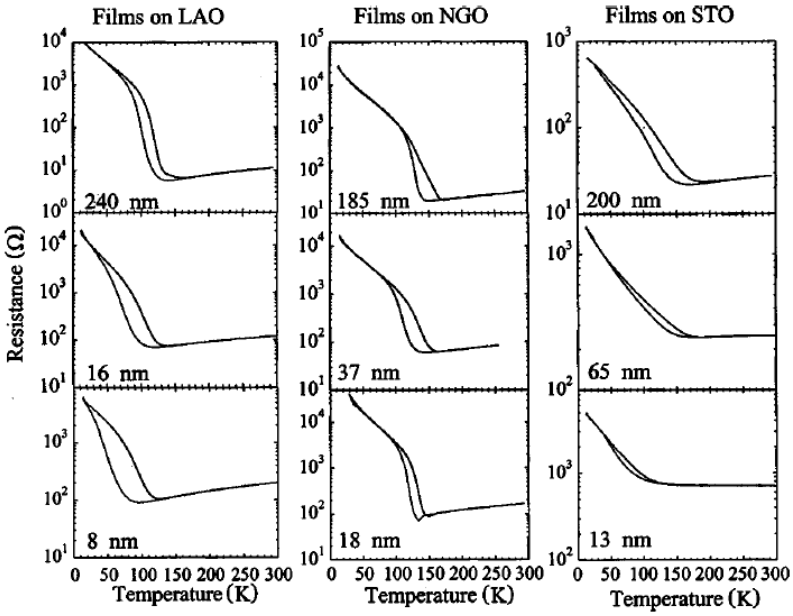

Figure 2.8: Resistance behaviour of $NdNiO_3$ thin films of varying thicknesses on the commonly used substrates $LaAlO_3$ (LAO), $NdGaO_3$ (NGO), and $SrTiO_3$ (STO). The metal-insulator transition temperature and hysteresis show some dependence on substrate lattice mismatch and film thickness. Reproduced from Figure 4 of Catalan et al. (2000) *Phys. Rev. B.* **62**(12) 7892-7900.

2.2.3 Crystal Growth Techniques

In the most general terms, thin film growth techniques deposit the constituent atoms of the growing film from a target and/or from the chamber atmosphere onto a substrate [28]. The precise manner in which the atoms are removed from the target and directed toward the substrate is the main distinction between most techniques. Additional distinctions arise from the type and number of targets, type and geometry of substrate, and chamber conditions including temperature, pressure, and magnetic field. Epitaxial growth techniques are those wherein crystallization is ordered along a crystallographic orientation determined by the properties of the substrate. This broad category includes techniques wherein crystallization occurs from the vapor, liquid, and solid phases, but we will only be considering vapor deposition here. In particular, we are interested in pulsed laser deposition and molecular beam epitaxy.

The thin film samples used in the XAS and STXM studies to be discussed in this thesis

were grown by pulsed laser deposition (PLD) on nanosheets. In PLD, the target is a sintered pellet matching the desired film stoichiometry. The target is vaporized by laser ablation using an excimer laser, most commonly a KrF laser ($\lambda = 248nm$) of pulse energy 1 – 2 J cm^{-2} and repetition rate of 1 – 4 Hz [25]. Nanosheets are prepared by exfoliating monolayers from a high quality bulk crystal. These sheets can be floated onto support structures like wafers or grids using techniques like Langmuir-Blodgett (LB) deposition [31] [32].

Molecular beam epitaxy (MBE) is a physical vapor deposition technique, meaning that the material to be deposited is vaporized and transported to the substrate by a gradient in either pressure or temperature. In MBE, the constituent atoms of the film are vaporized in separate effusion cells such that the deposition rates can be independently optimized. In effusion cells, a material is resistively heated in a sealed crucible with one small opening to the growth chamber. Once sufficient vapor pressure is achieved in the cell, a narrow beam of particles will enter the growth chamber through this opening.

During growth, the film is monitored by in situ reflection high energy electron diffraction (RHEED) wherein a beam of electrons strikes the sample at grazing incidence and the diffracted electrons form a pattern on a fluorescence screen. The diffraction pattern and quality provide insight into the growing film's crystallographic orientation and morphology [33].

Successful growth is a result of the complex interplay between the molecular beam fluxes, atmospheric variables, and substrate variables. For films where multiple molecular beams are used, it is important to balance the flux to achieve the desired stoichiometry. Process gas species (for oxides – molecular oxygen, ozone, or an ionized form), purity, and pressure are also significant factors in the final film stoichiometry. Substrate considerations include temperature, lattice spacing, orientation, surface termination, morphology, and roughness.

At high substrate temperatures deposited atoms may re-vaporize and escape the growing film. In instances where the constituent atoms have significant differences in vapor pressure, this may result in films with undesired stoichiometry. At low substrate temperatures growth

may occur in islands with inadequate diffusion across the surface to form smooth uniform layers.

Substrates with rough surfaces may cause polycrystalline domains or even amorphous films. Steps and dislocations in the substrate may 'print' through to the growing film. Substrates are typically polished wafers cut at particular orientations from bulk crystals. Prior to growth, these wafer substrates may be etched to ensure a desired surface termination and are annealed to remove volatile surface contaminants. In the MBE study described here, we use commercially grown and finished wafers of $(LaAlO_3)_{0.3}(Sr_2TaAlO_6)_{0.7}$ with a (100) crystal orientation (hereafter referred to as LSAT).

As previously mentioned, the final film stoichiometry is a crucial measure of the success of the growth process. This parameter can be evaluated by various spectroscopy methods. In this work we will primarily discuss XPS. As briefly discussed in Section 2.1.1, XPS can employ synchrotron radiation but it is more commonly a technique which uses either a Mg or Al K_α anode source with a high quality crystal monochromator. In XPS, a highly monochromatic x-ray beam is focused onto the sample surface and the ejected photoelectrons are detected by a hemispherical analyzer. The analyzer consists of an inner and outer hemispherical electrode pair which causes deflection in the path of the entering photoelectrons based on their kinetic energy. Subtracting this kinetic energy and a calibration factor from the probe photon energy gives the binding energy. Analysis of the signal intensity vs binding energy provides information about the elements present in the sample as well as their chemical state. XPS is ideal for identifying impurities and studying surface chemistry.

3 ELECTRIC AND MAGNETIC PROPERTIES OF A FREESTANDING $NdNiO_3$ THIN FILM

In Chapter 1 we briefly touched on the work already done to identify nanoscale phase separation in $NdNiO_3$ thin films. Different authors report varying transition temperatures and rate of transition (over how large a temperature range does the transition occur), but this is typical of $NdNiO_3$ thin films with differing film thickness and lattice mismatch with the growth substrate [7]. These values are provided in Table 3.1. In examining nanoscale phase separation, reports have also varied in terms of the size of observed metallic and insulating domains as well as their ordering, morphology, and behaviour.

In a 2016 study employing nano-IR, Post et al identified sub-micron sized domains with some ordering but no correlation with the film topography in a 20 unit cell (u.c.) thick NNO film [10]. Using X-PEEM on an 11 u.c. thick NNO film, Preziosi et al observed domains of 5-20 nm in diameter with no particular pattern or structure which displayed a stochastic character, appearing and disappearing without fixed position [8]. In another X-PEEM study on a 20 u.c. thick film by Mattioni et al, the domains observed were 100 to 150 nm in size and were ordered along film terraces [9].

Although each of these groups observed some form of separation of metallic and insulating domains, the degree to which these reports vary qualitatively and quantitatively is a motive for further investigation, particularly employing less surface sensitive techniques as discussed in Chapter 1.

3.1 Experiment

Here we discuss a series of experiments conducted on a single sample of a freestanding $NdNiO_3$ thin film grown by collaborators. A freestanding film of this type has not been

Table 3.1: Comparison of $NdNiO_3$ film studies - thickness and T_{MI}

NNO Film Thickness	Substrate	Capping Layer	T_{MI} Cooling [K]	T_{MI} Heating [K]
10 u.c.	LAO (001)	None	100 K	125 K [34]
11 u.c.	LAO (001)	None	63 K	90 K [8]
30 u.c.	NGO $(001)_{pc}$	None	150 K	178 K [9]
20 u.c.	NGO $(001)_{pc}$	1.5 nm LAO	159.3 K	172.4 K [10]
138 u.c.	CNO Nanosheet	None	145 K	150 K

fabricated previously, so characterization of the film's electronic and magnetic properties was of particular interest. This film geometry also permits a less surface sensitive examination of the separation of electronic phases through the metal insulator transition.

The growth method and initial characterization results are described in subsection 3.1.1. Subsequent work was conducted at the CLS at the SM beamline and at the REIXS beamline. We present XAS results from room temperature down to 100 K on heating and cooling, showing the metal insulator transition in the bulk of the film as well as the results of STXM experiments aimed at observing the formation of insulating and metallic domains as the transition progresses. We also present x-ray magnetic scattering results over the same temperature range, showing the antiferromagnetic transition concurrent with the electronic transition.

3.1.1 Thin Film Preparation and Characterization

The $NdNiO_3$ thin film sample used in this study was grown by collaborators at the University of Twente using pulsed laser deposition (PLD). The substrates for this film growth consisted of $Ca_2Nb_3O_{10}$ (CNO) nanosheets supported by transmission electron microscope (TEM) grids placed in the window regions of a commercial TEM microchip, shown in Figure 3.1 with each window (henceforth referred to as a sample pad) labelled for reference. The individual features of the films at each sample pad are shown in Figure 3.2.

The CNO nanosheets were fabricated by chemically exfoliating layers from crystalline $KCa_2Nb_3O_{10}$ (KCNO). KCNO is a layered perovskite in which the CNO layers alternate

with layers of potassium ions. This compound can be treated with nitric acid (HNO_3) to replace the potassium with hydrogen ions, an ion-exchange reaction process known as protonation. The protonated product, $HCa_2Nb_3O_{10}$ (HCNO), can then be treated with tetrabutylammonium hydroxide (TBAOH) which captures the hydrogen ions from the HCNO, leaving negatively charged CNO sheets suspended in solution [30] [35] . These sheets can then be deposited by the Langmuir-Blodgett method–a technique relying on suspension of amphilic particles or nanosheets at the liquid-air interface [31] [36]. A sliding block applies compressive force to the film at the interface and a substrate is either dipped into or lifted out of the solution. As the substrate is lifted, the film sticks to the surface. This technique produces monolayered films of the nanosheets, but the morphology is not perfectly smooth as the nanosheet fragments vary in size and shape and thus may pack imperfectly. Different approaches to the initial KCNO synthesis and to the exfoliation process have yielded nanosheets of varying shape, size, and quality [37]. Individual nanosheet platelets are typically between 1 µm and 20 µm in width [32].

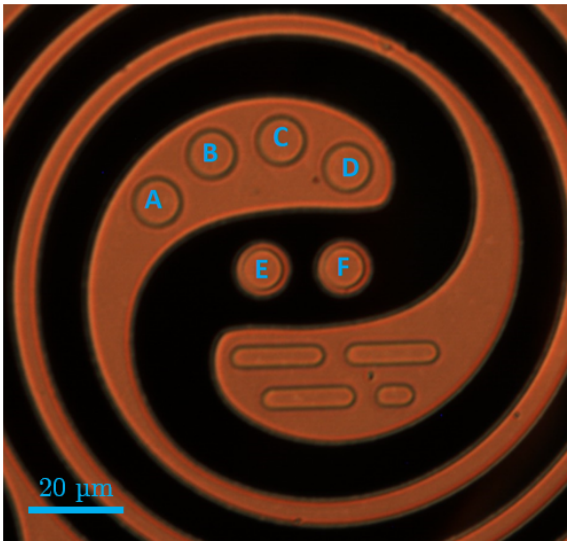

Figure 3.1: $NdNiO_3$ thin film on commercial TEM microchip imaged with a visible light microscope.

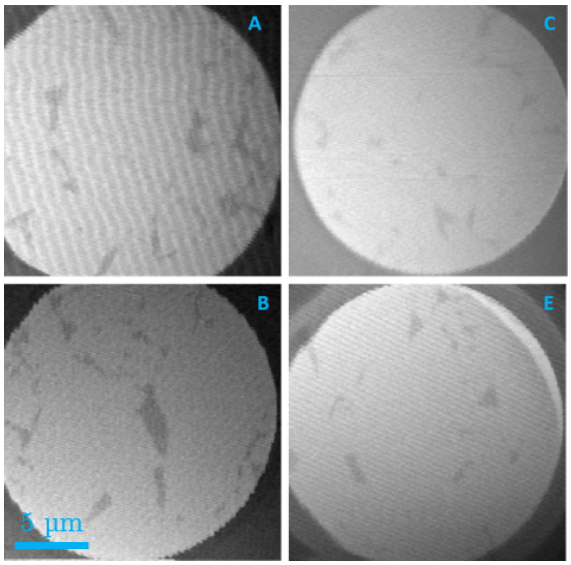

Figure 3.2: Scanning transmission x-ray microscope (STXM) images of individual sample pads at E = 852.8 eV. This energy is used as it provides a high contrast between the high quality continuous regions and the defect regions of the sample.

The grown films were imaged by collaborators at the University of Antwerp using scanning transmission electron microscopy (STEM) at a variety of magnifications from a 9 µm by 9 µm field of view (FOV) to an 18 nm by 18 nm FOV with sub-nm resolution. Two representative STEM images are shown in Figure 3.3. In the high magnification images, good epitaxy with the correct stoichiometry (confirmed by electron energy loss spectroscopy (EELS) maps collected at the same time as the STEM images) can be seen in most places. The nanoscale defects visible in these images can be separated into two categories: NiO phases and Nd_2NiO_4 phases. In both of these defects the nickel is in the 2+ oxidation state, whereas in the desired composition, $NdNiO_3$, we have Ni^{3+}. As these oxidation states are distinguishable in XAS spectra we can readily identify the defect and non-defect spectra, but the two types of defects are not distinguishable from one another.

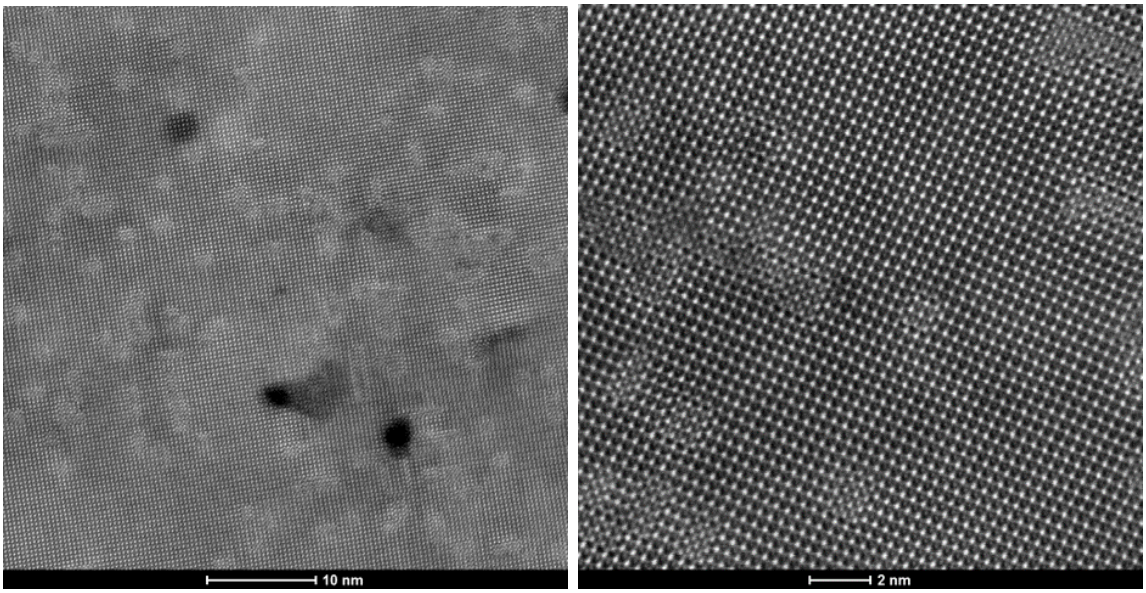

Figure 3.3: STEM images of $NdNiO_3$ film as grown. Dark spots correspond to NiO defects. Light spots correspond to RP phase defects (Nd_2NiO_4). Images courtesy of N. Gauquelin, University of Antwerp.

3.1.2 XAS

All XAS data presented here was collected at the CLS at the REIXS beamline using the resonant soft x-ray scattering (RSXS) endstation. In order to enable direct detection of the transmitted beam, the sample was mounted over a hole in the standard sample holder. To accommodate the high intensity associated with detecting transmitted x-ray signal rather than x-ray fluorescence or electron yield, the beam was detected downstream of the sample using a photodiode detector. The relative intensity of the incoming beam, I_0, is detected by an in-line gold mesh upstream from the sample. The current at the mesh is approximately proportional to the beam intensity and can be used to normalize for variation in beam intensity during each scan.

The sample was cycled from approximately room temperature down to a minimum of 100 K and back up to room temperature with temperature increments of 10 K in the range of the metal insulator transition (210 K to 140 K) in order to observe the hysteresis in the film. The scan energy range was from 830 eV to 890 eV to capture the nickel L_3 and L_2 absorption edges.

An initial scan was collected with the sample out of the beam path to establish a baseline intensity for the direct beam on the photodiode. To convert the transmission data for each scan to absorption, we divide the intensity, I, by the direct beam intensity, I_0 and take the negative log of this quotient. For each scan, we subtract the linear best fit to the pre-edge (830 eV <E <844 eV) and normalize to the average value of the post-edge (880 eV <E <890 eV).

3.1.3 STXM

The spectromicroscopy experimental work was done at the SM beamline at the CLS using the cryo-STXM apparatus. In this instrument's geometry, the beam enters from the left and is focused onto the sample by a zone plate and an order selecting aperture. The sample is rastered through the beam and the transmitted x-rays are detected by a scintillator coupled to a photomultiplier tube (PMT) as shown in Figure 3.4 [17]. In this case, we do not have a pre- and post-sample ion chamber to collect I_0 and the transmitted beam. Ideally, a sample for this method would have a small hole / non-sample void somewhere within the field of view to allow for each frame (image within the stack) to be normalized to the direct beam, but that was not possible in this case.

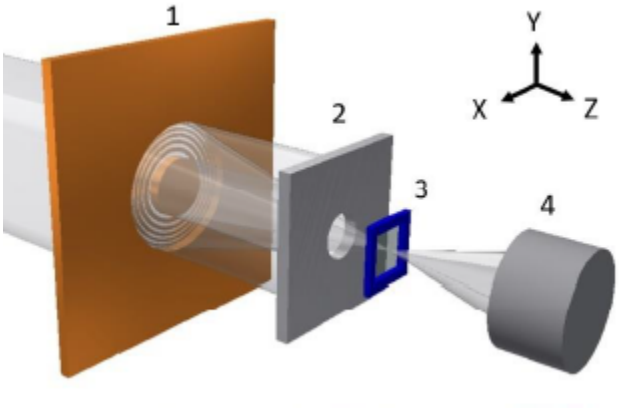

Figure 3.4: Schematic of cryo-STXM beam path showing the incoming beam at the left focusing through the zone plate (1), order selecting aperture (2), sample (3), and ending at the detector (4). Figure from Leontowich et al (2018) [17].

Prior to cycling the sample through the full temperature range, we verified that the sample displayed the expected high temperature and low temperature spectra with quick, low resolution scans at room temperature and at 93.15 K, well below the metal insulator transition. For the higher resolution data collection, the sample was allowed to equilibrate for at least 10 minutes at each temperature prior to beginning the scan. Stack scans were performed from 93.15 K to 223.15 K in increments of 10 K. Each stack scan consists of a series of images of dimension 8 µm by 8 µm with a step size of 50 nm, with each image at a different x-ray energy. An individual sample image from a room temperature STXM stack scan is shown in Figure 3.5.

The spectral region of interest in this experiment was the nickel L_3 edge, so the scan energies ranged from 845 eV to 855 eV with a higher density of data collection points from 850.2 eV to 855 eV. The set of these images is a “stack". Since the same sample area is imaged at each energy, each pixel can be considered to have an associated XAS spectrum. Regions of differing spectral character can then be mapped and compared. In this experiment, we hoped to see distinct domains matching insulating and metallic spectra form as the sample was heated through the metal insulator transition.

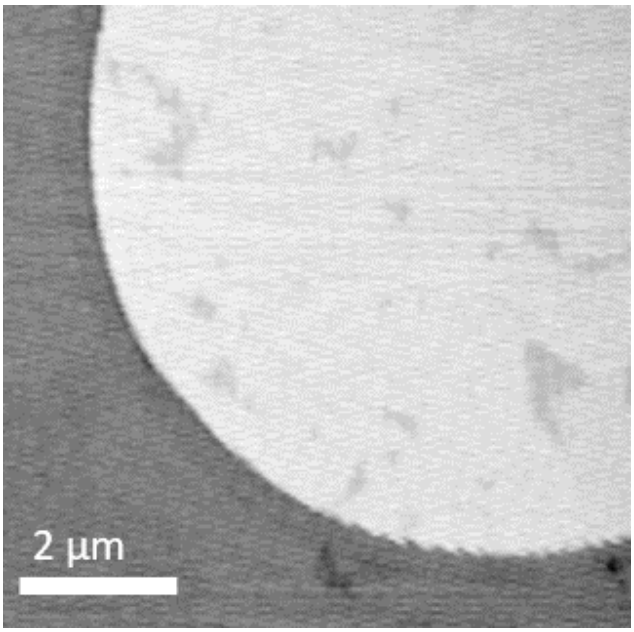

Figure 3.5: An individual sample image from a STXM stack scan at 293.15 K. This image was taken at a beam energy of 852.8 eV. The light continuous region within the circular sample pad area matches reported spectra for $NdNiO_3$ samples. The darker, discontinuous regions within this area fit to a distinct spectrum which does not vary with temperature.

3.1.4 Magnetic Scattering

Both the XAS and STXM experiments were aimed at characterizing the electronic behaviour of this unusual $NdNiO_3$ thin film sample–identifying the approximate metal-insulator transition temperature, quantifying the hysteresis in this transition, and observing any discontinuities or spatial inhomogeneity in the transition. As an additional characterization measure, we conducted a resonant x-ray diffraction experiment to examine the magnetic behaviour of the sample. $NdNiO_3$ displays antiferromagnetism at low temperature with a Néel temperature (magnetic transition temperature) concurrent with the metal-insulator transition temperature as shown in the phase diagram Figure 2.5 in Chapter 1.

In the bulk, $NdNiO_3$ antiferromagnetism is achieved by the cancellation of repeating pattern of four ferromagnetic layers aligned to the 111 (pseudocubic) lattice vector [38]. This magnetic ordering can be detected with resonant x-ray diffraction at the Ni L_3 edge [39].

The intensity of the observed diffraction peak can be used to track the magnetic transition, particularly the magnetic order parameter and the Néel temperature [26].

3.2 Results and Analysis

3.2.1 XAS

XAS spectra were collected across the Ni L_3 and L_2 edges on heating and cooling from 300 K to 100 K. The results on cooling are presented in Figure 3.6. As expected, we see splitting of the L_3 peak (at approximately 853 eV) with decreasing temperature. This feature serves as our indicator of the progress of the electronic phase transition from metallic to insulating. The L_2 peak also undergoes some change over this range, however it is subtle and only really distinctive at the extremes of temperature so we do not rely on it as a marker.

Figure 3.7 shows both heating and cooling data over a narrower range centered on the Ni L_3 edge. At each temperature the peak shapes are similar on heating and cooling, except for some broadening on the leading edge (850 eV to 852 eV) in the cooling results. This is particularly evident at increasing temperatures.

To quantify the progress of the metal insulator transition, we turn to principle component analysis, identifying a characteristic metallic spectrum and a characteristic insulating spectrum to be combined linearly to fit all the intermediate spectra. We define the "metallic" spectrum to be the best quality spectrum available at the highest temperature and the "insulating" spectrum to be the best quality spectrum at the lowest sampled temperature. In this section and in our discussion of the STXM results, we refer to this process as fractional fitting. In Figure 3.8 the selected metallic and insulating reference spectra used in fractional fitting are shown.

In Figure 3.9 the results of fractional fitting are shown. For each temperature, the coefficients found for each component in the best fit are plotted. We see a clear transition from metallic to insulating behaviour with a small, but distinct hysteresis. This hysteresis is similar to that observed in thin films of $NdNiO_3$ grown on traditional wafers (see Figure 2.8), indicating that the electronic phenomena are preserved in this freestanding film geometry.

Thus, these XAS results are the first demonstration that $NdNiO_3$ films of this type could be deployed to achieve the same functionality as bulk $NdNiO_3$ in potential device applications.

We find the transition range to extend from 100K to 185K with T_{MI} of 145 K on cooling and 150 K on heating. We anticipated the metal insulator transition occurring at a higher temperature than observed in the XAS results, so the distribution of sample temperatures is not ideal. We define our 100 K spectrum to be the insulating state, but because we do not see the low-temperature, insulating state 'saturate', we cannot be certain that the transition is actually complete at this temperature. Should we have the opportunity to repeat this experiment, we would collect data below 100 K to clarify this point and at several intermediate temperatures between 100 K and 150 K to clarify the shape of the curve in this region.

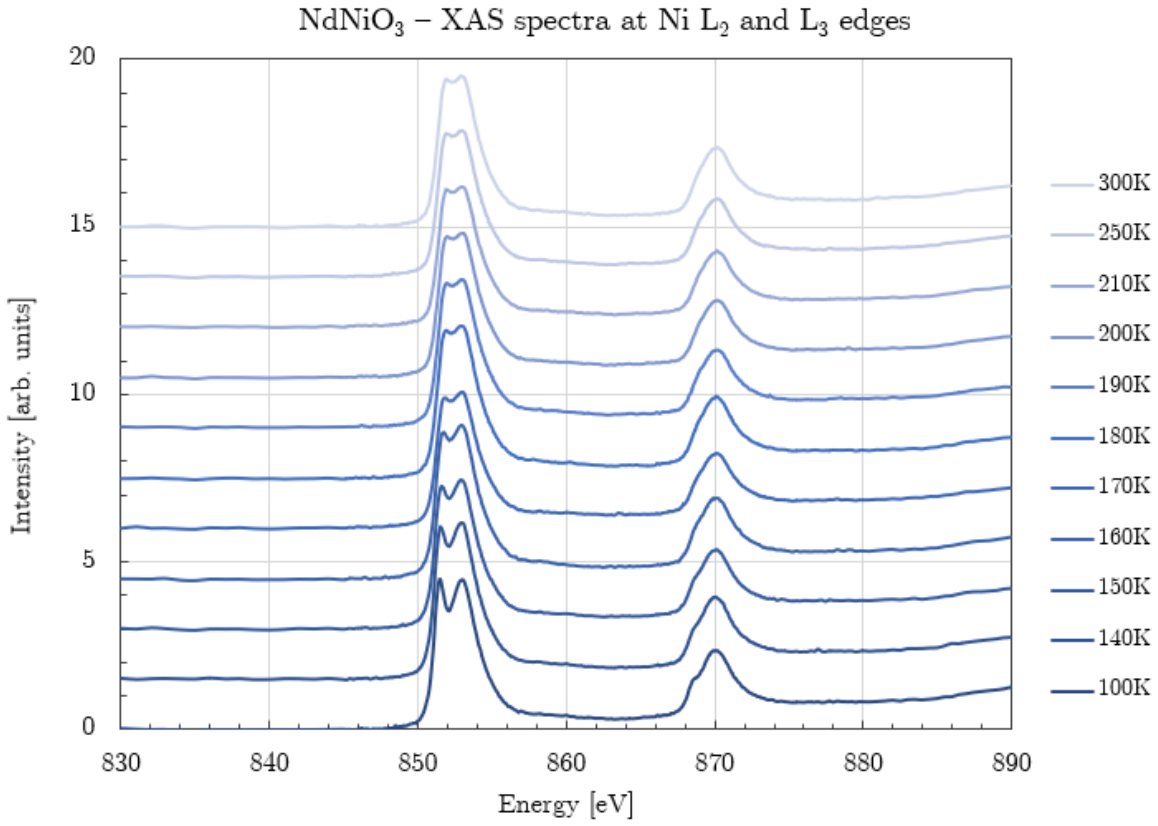

Figure 3.6: XAS spectra across the Ni L_2 (870 eV) and L_3 (853 eV) edges for a $NdNiO_3$ sample on cooling from 300 K to 100 K. Spectra are vertically displaced from one another on the chart for clarity.

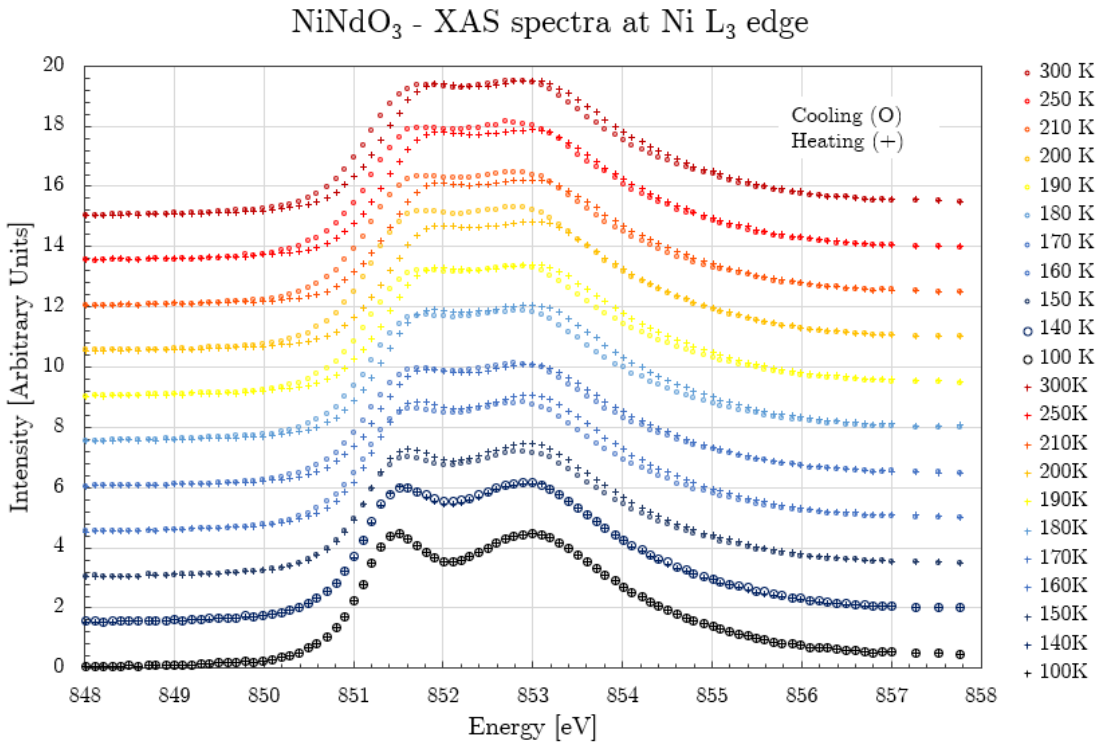

Figure 3.7: XAS spectra across the Ni L_3 edge for a $NdNiO_3$ sample for the full temperature cycle cooling from 300 K to 100 K and heating back up to 300 K. Spectra are vertically displaced from one another on the chart for clarity with spectra at the same temperature overlaid.

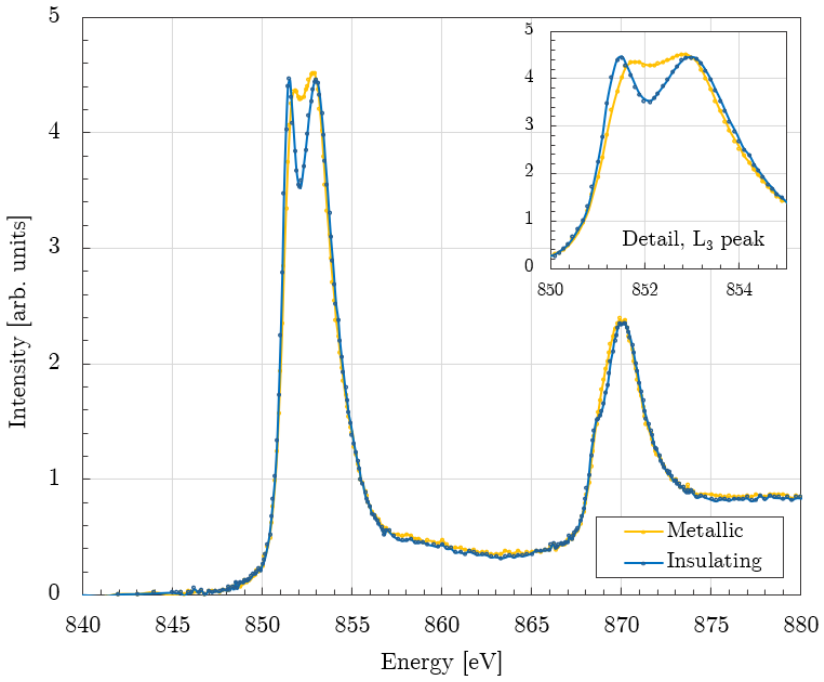

Figure 3.8: Metallic and insulating XAS spectra used as references for fractional fitting of the spectra at intermediate temperatures to track the progression of the metal insulator transition. Each intermediate spectrum is treated as a linear combination of the metallic and insulating spectra.

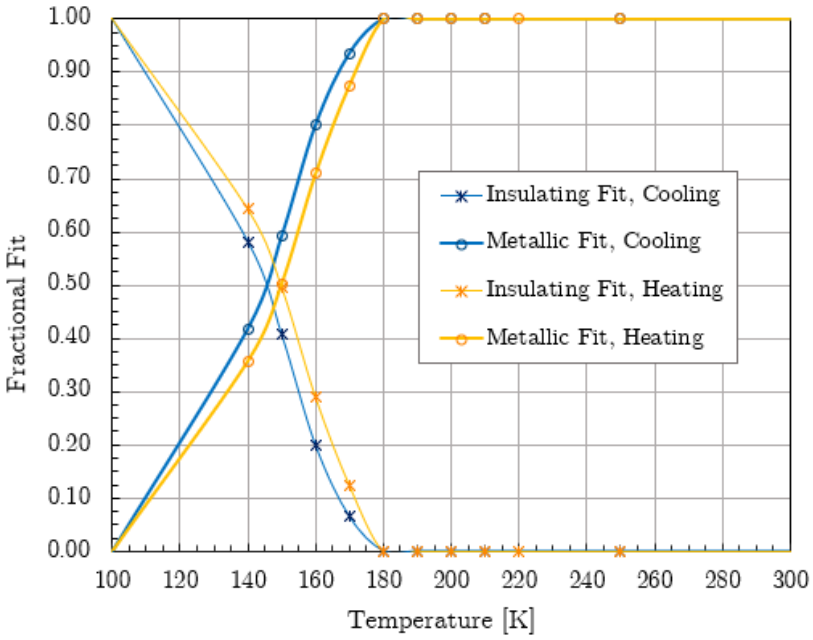

Figure 3.9: Fractional fitting results on heating and cooling the sample. A fit value of 1 corresponds to a perfect fit to the specified spectrum. For a two component fit, a fractional fit value of 0.5 corresponds to an equal spectral contributions from the metallic and insulating phases.

3.2.2 STXM

XAS spectra extracted from STXM results are presented in Figure 3.10. In the absence of direct beam data, these spectra cannot be normalized to the same standard. Instead, we have simply plotted the negative log of the signal intensity to convert from transmission to absorption, subtracted a linear background fit to the pre-edge, and scaled the peaks to an arbitrarily chosen maximum. There is substantial variation in the edge jump for each stack which presents some challenges in later stack fitting efforts, but the gradual peak splitting at the Ni L_3 edge as the sample temperature is reduced corresponding to the shift from metallic to insulating character is readily discernible.

This transition is quantified in much the same manner as the XAS results discussed in the preceding section: representative "metallic" and "insulating" spectra from the highest and lowest temperature scans respectively are used as components in a linear combination to

find the best fit to each spectrum. For the STXM results, however, the best quality fits were achieved by including a third, "defect", spectrum as a fit component. The defect spectrum is extracted from small regions whose spectra display one sharp peak with Ni^{2+} character and do not display a temperature dependence, as shown in Figure 3.11.

The selected reference spectra used in fractional fitting are presented in Figure 3.12 and the fractional fitting results are shown in Figure 3.13. We find a transition range from 130 K to 170 K with a T_{MI} of 150 K on heating, which is consistent with the results from the XAS collected at REIXS and within the range of reports in the literature (see Table 3.1). The modest variance in the share of the defect spectrum fit can most likely be attributed to the variation in edge jump in the STXM spectra which introduced errors into the fitting. Consequently, although the STXM fit agrees with the XAS fit results, we deem the XAS to be the more reliable metric based on the more consistent edge jump in the spectra across the full temperature range.

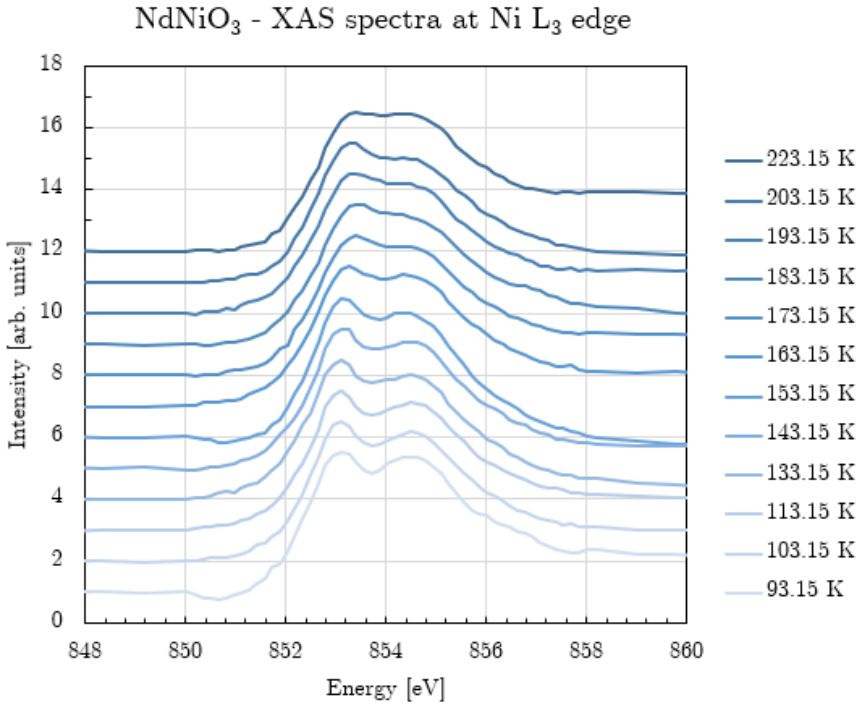

Figure 3.10: XAS spectra at the Ni L_3 edge extracted from STXM results for $NdNiO_3$ sample on heating from 93.15 K to 223.15 K. The presented spectra are average values for all pixels within the "continuous", non-defect regions of the sample pad.

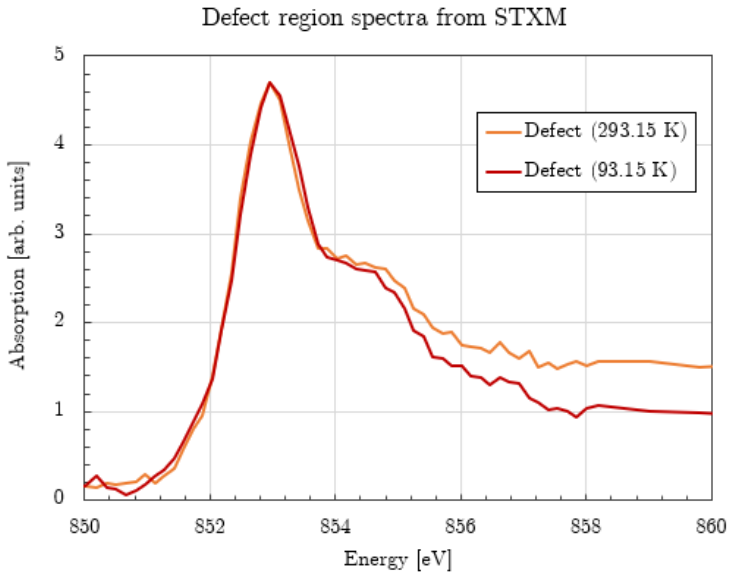

Figure 3.11: XAS spectra at the Ni L_3 edge for defect regions at 293.15 K and 93.15 K. Spectra are normalized to an arbitrary maximum value. Although there is variation in the edge jump in spectra across the entire temperature range, the defect peak shape and position are consistent.

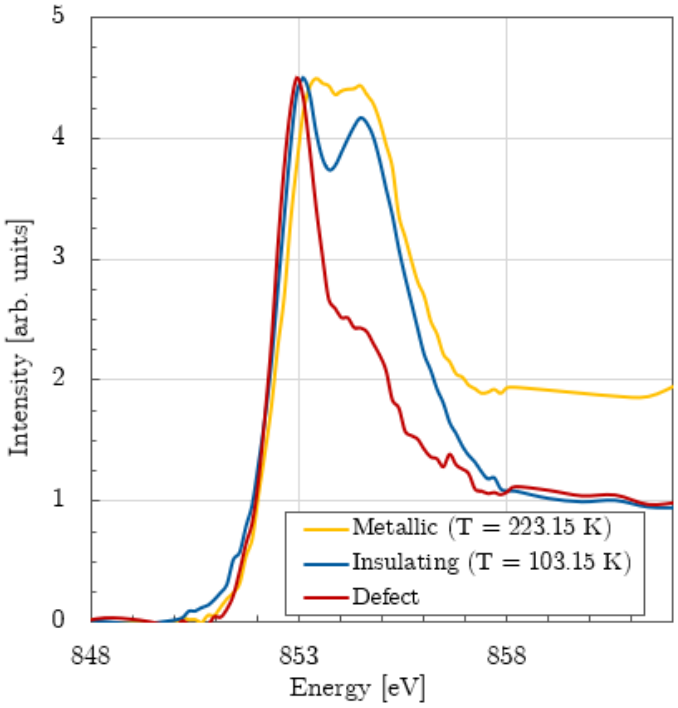

Figure 3.12: Metallic, insulating, and defect XAS spectra used as references for fractional fitting of the spectra at intermediate temperatures to track the progression of the metal insulator transition. Each intermediate spectrum is treated as a linear combination of the metallic, insulating, and defect spectra.

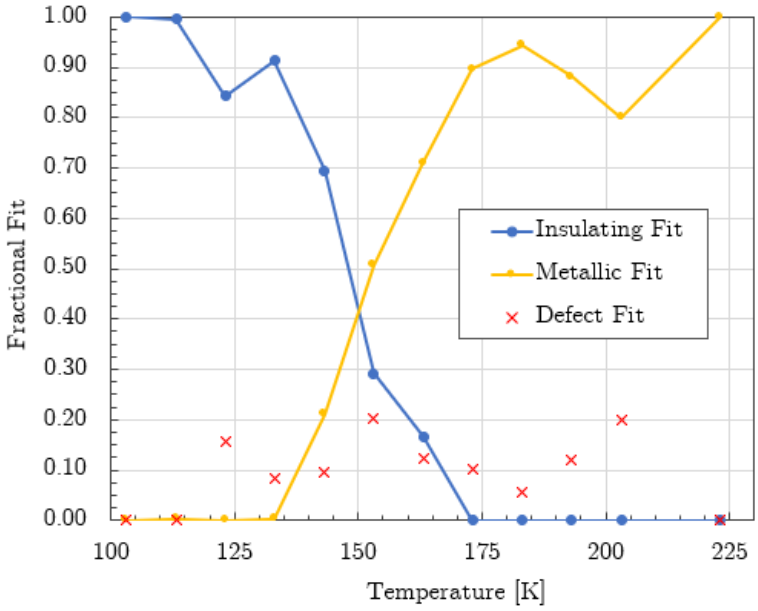

Figure 3.13: Fractional fitting results for sample on heating. A fit value of 1 corresponds to a perfect fit to the specified spectrum. Acceptable fit quality could only be achieved using a three component fit (including the defect spectrum).

SVD Mapping

In the XAS results, we can clearly see the progression of the metal insulator transition as well as a moderate hysteresis (see 3.9). The next question to approach is whether the transition progresses uniformly over the entire area of the sample with the film gradually shifting from the low temperature insulating phase to the higher temperature metallic phase or whether there is granularity. If the latter is true, we should be able to identify distinct metallic and insulating phase domains in the STXM results. To verify this, we applied singular variable decomposition (SVD) mapping to each stack. Initial attempts using only two components (metallic and insulating spectra) were unsuccessful. Adding a third, defect, component improved the fit quality substantially. For best results, STXM stacks were cropped to include only the sample pad area and reference spectra were chosen for best match to the stack edge jump while still displaying strong metallic or insulating character.

In Figure 3.14, an SVD map is shown for a stack at 183.15 K. At this temperature, the film should be dominantly metallic and we would anticipate a good fit to the metallic

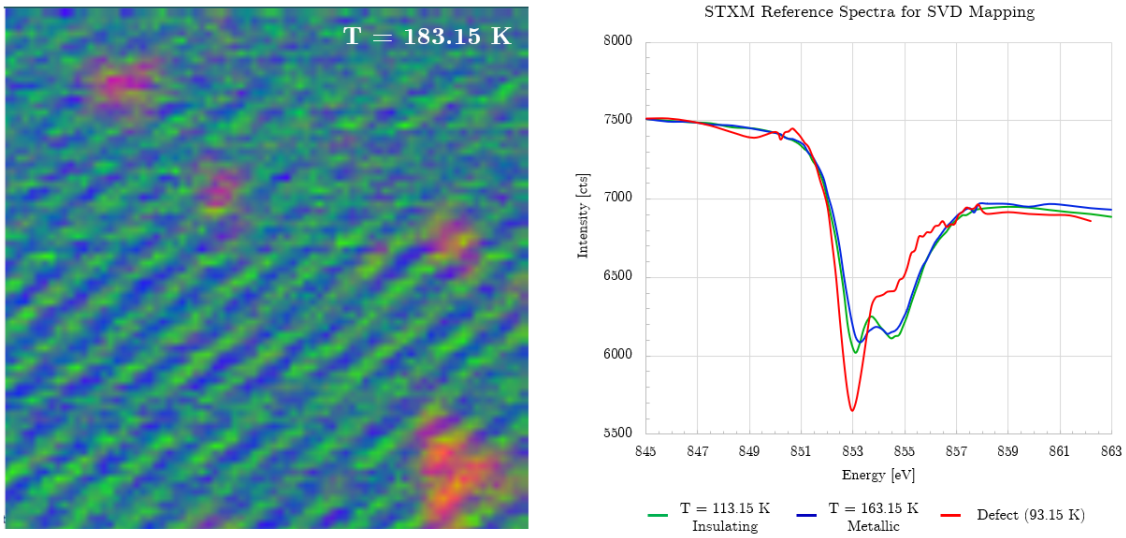

Figure 3.14: At left, an overlay of the SVD component fit maps for a STXM stack at T = 183.15 K to the insulating (green), metallic (blue), and defect (red) spectra shown in the plot at the right. To improve fit quality the insulating, metallic, and defect spectra were chosen for having similar edge jumps.

spectrum throughout as well as patches of defects. Instead, we see an excellent fit to the defect spectrum in the expected areas and approximately equal amounts of metallic and insulating in the non-defect regions. Further, the metallic and insulating fit maps have a consistent periodic rippling character which matches a feature observed in the raw STXM images (Figure 3.15).

Spatially separated domains were not observed. If domains are present, they may not be uniform through the depth of the sample as illustrated in Figure 3.16. Alternatively, any distinction between domains may be obscured by periodic noise.

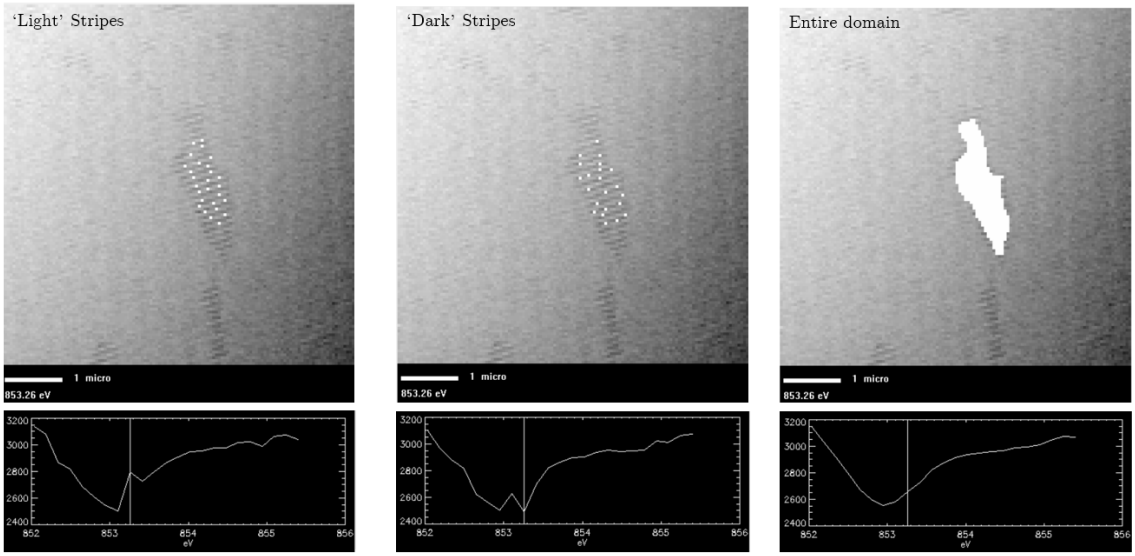

Figure 3.15: Average spectra can be isolated from chosen sets of pixels. In the above images, a set of pixels indicated in white are selected to compare the XAS spectra corresponding to what appears to be periodic noise. At left and centre are the results for the contrasting periodic stripes. At right is the result for averaging over the entire area. In each case, a representative spectrum can be constructed from only a few pixels and the addition of more from the same stripe makes no difference. A smooth spectrum only presents if pixels from both stripes are included in the average. This suggests that the periodic stripes observed are noise rather than actual sample features.

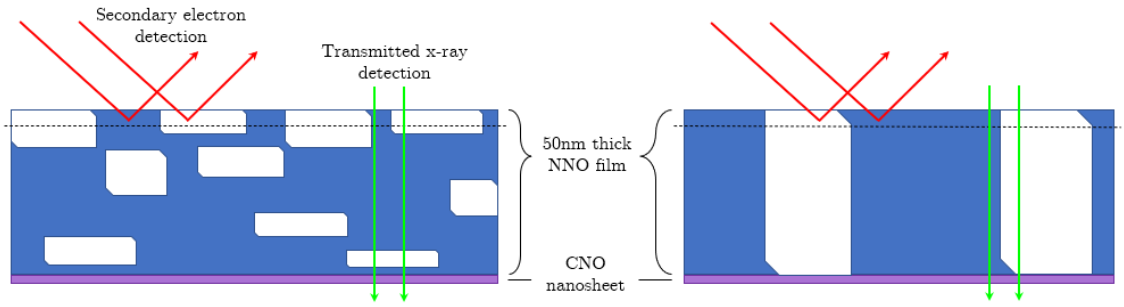

Figure 3.16: Hypothetical domain shapes. Since the domain sizes reported by other workers range between 5 nm and approximately 200 nm, it's possible that in our 50 nm thick film, the domains do not penetrate the entire depth. Thus, when viewed in transmission we may collect an averaged signal of both metallic and insulating domains in the transition range.

Periodic Artifacts

Periodic noise is a common problem in STXM images and there are many potential sources ranging from the booster ring itself to scan parameters at the beamline. Periodic noise of several amplitudes was consistently present in our STXM results, but could not be reliably traced to a identifiable source. Although we had some success using FFT filtering to remove these artifacts in individual images, the results were not sufficiently improved to merit application to the full stacks (Figure 3.17).

3.2.3 Magnetic Scattering

For a fuller picture of the properties of a freestanding $NdNiO_3$ thin film, we complement our examination of the electronic properties with a synchrotron study of the magnetic properties. At elevated temperatures (greater than 200 K), bulk $NdNiO_3$ is paramagnetic (see Figure 1.3). Below this temperature it is antiferromagnetic. In this study, we collected magnetic scattering data from a minimum temperature of 30 K, heating the sample in increments of 10 K until the magnetic Bragg diffraction peak vanished indicating a paramagnetic state. These results from 30 K to 190 K are presented in Figure 3.18. The peak is non-existent at temperatures over 180 K and steadily increases in intensity with reduced temperature,

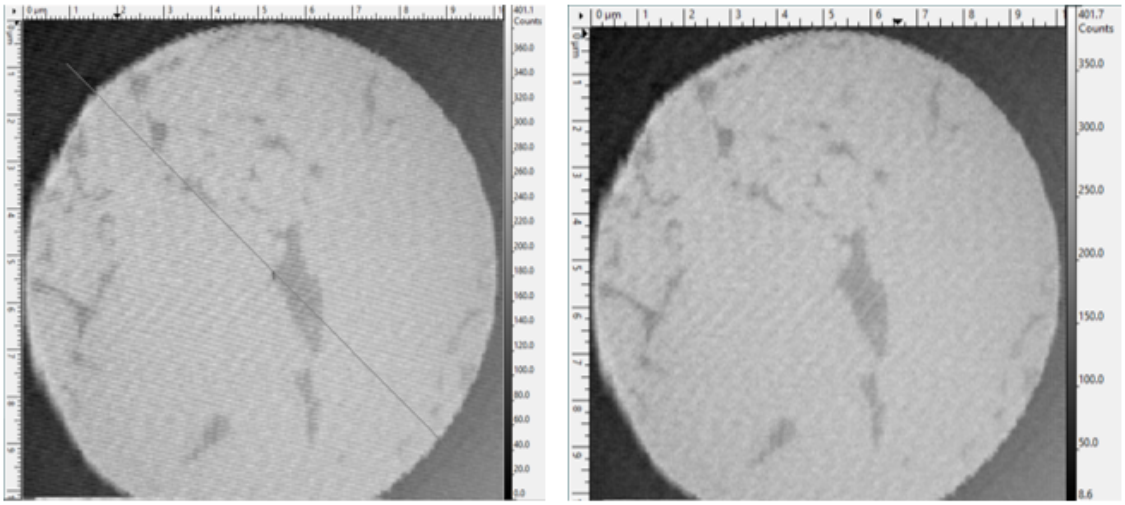

Figure 3.17: At left, a raw STXM image displaying periodic noise. At right, the same image after processing using the 2D FFT filtering function in the Gwyddion software package [40]. Although there is some reduction in noise, periodic artifacts are still present.

reaching a maximum at approximately 80 K. This is most clearly visible in Figure 3.19, which shows the integrated magnetic scattering intensity at each temperature.

The magnetic transition is approximately halfway complete at 130 K to 150 K, matching well with the electronic transition observed by XAS and STXM in this sample at 145 to 150 K. As in bulk samples of $NdNiO_3$, the electronic and magnetic transitions are concurrent, though they occur at a slightly depressed temperature.

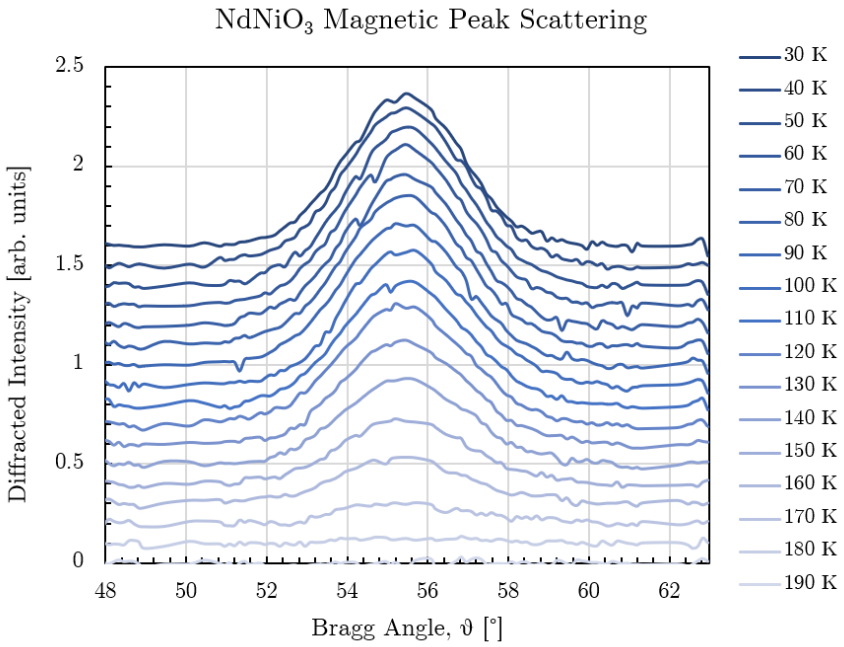

Figure 3.18: Magnetic Bragg diffraction peaks.

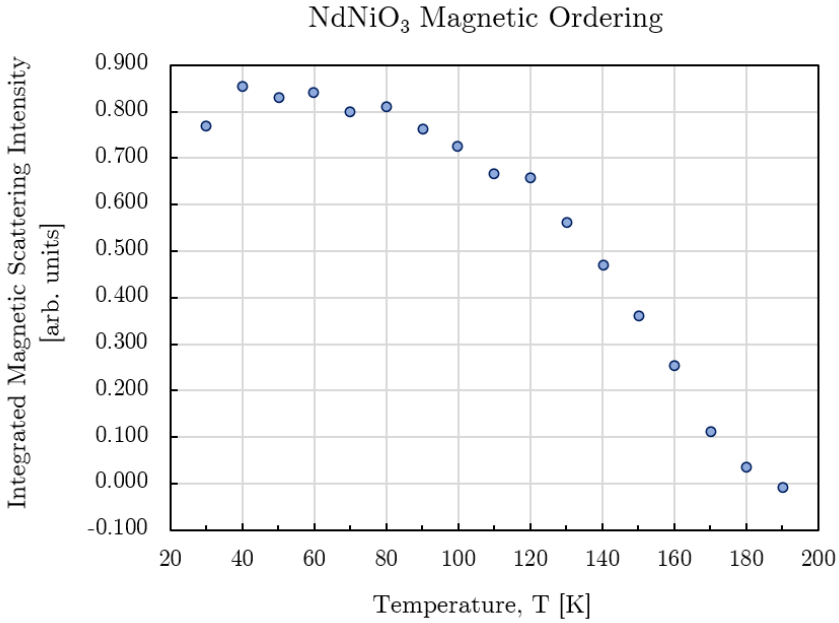

Figure 3.19: $NdNiO_3$ magnetic ordering.

4 GROWTH OF $SmTiO_3$ THIN FILMS

In this chapter, we present the results of a series of epitaxial growth runs targeted at producing high quality $SmTiO_3$ thin films. These films are of interest for study as layers in heterostructured films wherein interface effects are examined. In particular, a recent study found a strong charge carrier density dependence in the metal insulator transition at a thin film interface between $SmTiO_3$ and $SrTiO_3$. This type of tunable electrical behaviour is naturally of great interest in computing applications.

4.1 Experiment

All film growth was conducted at the REIXS beamline Surface Science Facility (SSF) at the CLS using the molecular beam epitaxy (MBE) growth apparatus. The MBE chamber was configured for growth using two high temperature effusion cells containing titanium and samarium targets respectively with O_2 as the process gas. Deposition rates from the effusion cells were monitored using a quartz crystal monitor (QCM) and the O_2 partial pressure was monitored using an ion gauge detector. Due to instability in the flux from each effusion cell, the cell temperatures had to be adjusted prior to each growth run, but remained at approximately $T_{Sm} = 554$°C and $T_{Ti} = 1550$°C to achieve a growth rate of 0.5 monolayers/minute. Oxygen partial pressure during growth varied from 1×10^{-9} Torr to 2×10^{-9} Torr.

The growth substrates were commercially fabricated $(LaAlO_3)_{0.3}(SrTaAlO_6)_{0.7}$ (LSAT) wafers of dimensions 5 x 5 mm. The growth surface of these wafers was polished and oriented to the crystallographic (100) plane. Prior to introduction to the evacuated growth chamber, the substrates were baked on a hot plate for several hours at 220°C to remove volatiles from the surface. Once loaded into the growth chamber, the substrate temperature was increased to the growth temperature (800°C or 850°C depending on the trial) at a rate

of 20°C/minute. The substrate was left to equilibrate at the growth temperature for 1 hour before beginning deposition. During growth, the films were monitored by RHEED and after growth, the quality was evaluated using XPS.

4.2 Results and Analysis

4.2.1 RHEED

Here, RHEED is primarily employed as a diagnostic to ensure that growing film showed the expected periodicity, implying the correct crystalline habit as opposed to amorphous deposition. RHEED also enables monitoring of film morphology and roughness. Representative results are shown in Figure 4.1. Growth was crystalline, but uneven, tending towards the formation of islands. This is often an indication that the substrate temperature is too low, but at 850°C the apparatus was already at the maximum heater setting. Some improvement in quality was observed with slightly increased O_2 pressure, indicating that although the substrate temperature is limited with this MBE system, higher quality films might yet be achievable.

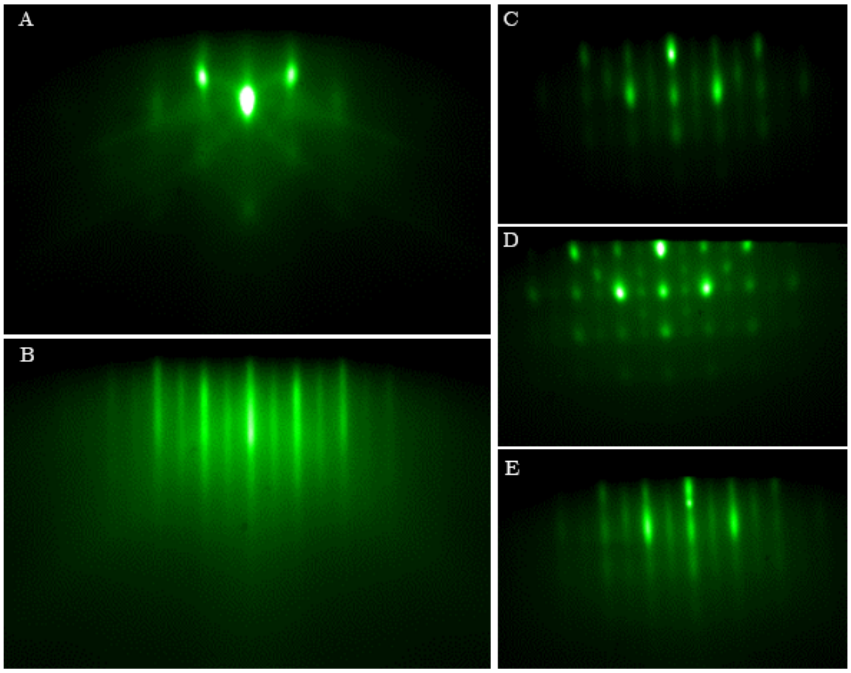

Figure 4.1: In situ RHEED images during MBE growth of $SmTiO_3$ thin films. **A.** LSAT(100) substrate heating to growth temperature (800°C) prior to growth run "smt01"; **B.** Film after 45 minutes of growth, cooled to room temperature after growth run "smt01". Vertical streaking indicates film unevenness/roughness. **C,D,E.** Varying sample regions after growth run "smt02", 33 minutes total deposition time. Substantial variation in film quality across the sample.

4.2.2 XPS

After growth, the film composition was evaluated using XPS with an Al K_α source. The films were kept under vacuum after growth and at no time were exposed to the ambient environment prior to or during XPS measurements.

The raw results of XPS are in terms of the kinetic energy of the ejected photoelectrons and for survey scans this ranges from a minimum energy of 200 eV to a maximum of the probe x-ray energy. In this case, the x-ray source is an Al K_α anode which has an energy of 1486.6 eV. The results are presented in terms of binding energy which can be found by calibrating in terms of the spectrometer work function, ϕ, and the probe x-ray energy. The relationship between photoelectron kinetic energy and the binding energy is given in Equation 4.1.

$$E_{binding} = E_{photon} - (E_{kinetic} + \phi) \tag{4.1}$$

Although more sophisticated analysis is possible with dedicated software to examine the peak shapes etc, in this work we did a simple manual comparison with the reported peaks of expected constituent elements as well as common contaminants (carbon in particular) [41].

X-ray photoelectron spectroscopy (XPS) of the grown films confirms their high purity – no organic contamination is visible in the spectra. The only notable spectral lines present can be attributed to samarium, titanium, and oxygen. Most of the lines indexed in Figure 4.2 are unambiguous, however the Ti LMM Auger series overlaps with the Sm 3d lines making it substantially less clear. If present, this could account for some of the variation in the spectra from 1068 eV to 1098 eV [41].

There is minimal variation in the oxygen and samarium peaks from growth run to growth run as shown in the detailed plots of the Sm 3d and O 1s peaks, Figure 4.3 and Figure 4.4 respectively. In Figure 4.5, however, we see a small difference in the separation of the Ti $2p_{1/2}$ and $2p_{3/2}$ peaks as well as the presence of shoulder-like features with varying intensity of expression. These shoulders can most likely be attributed to increasing abundance of Ti^{3+}, while narrower peaks indicate that Ti^{4+} is more dominant [42–44]. This variation in Ti oxidation state could be an indicator that the grown films are oxygen deficient or that there is some charge transfer at the interface. Further analysis is needed to make a clear determination of the electronic structure of the films grown.

The $SmTiO_3$ films grown in this study were of high quality in terms of composition, but there remains work to be done in optimizing growth conditions to improve the surface morphology. Unfortunately, this work was stalled due to interruptions in facility access caused by COVID-19.

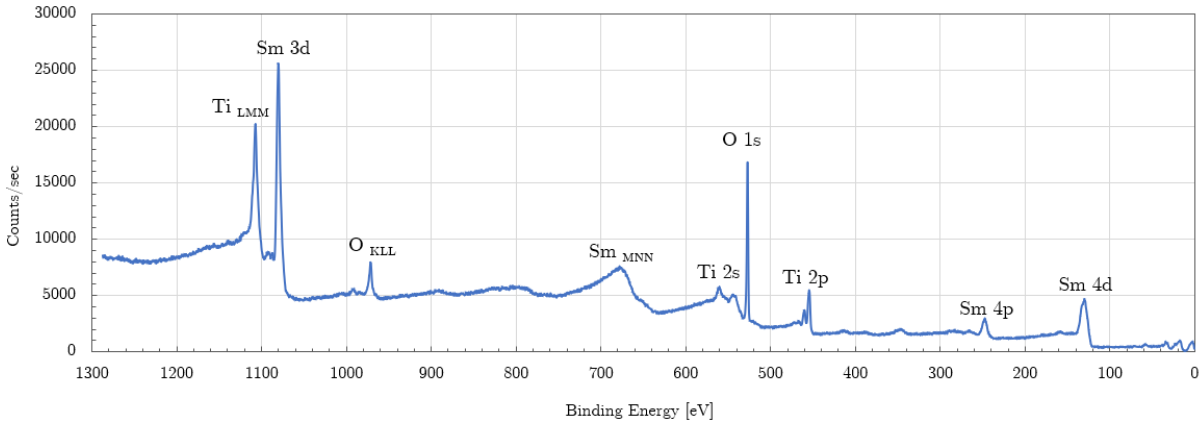

Figure 4.2: XPS survey scan for an $SmTiO_3$ film. All identified peaks are labelled with the corresponding transition.

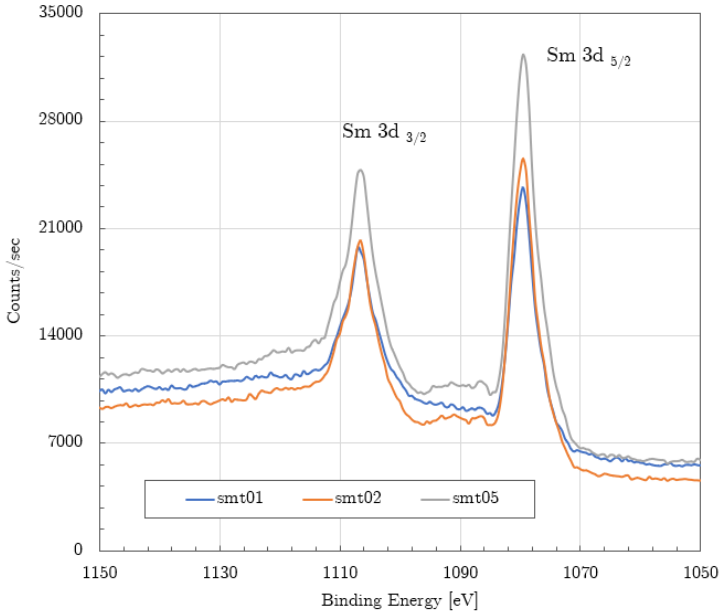

Figure 4.3: Comparison of samarium peaks in XPS spectra for several grown $SmTiO_3$ films.

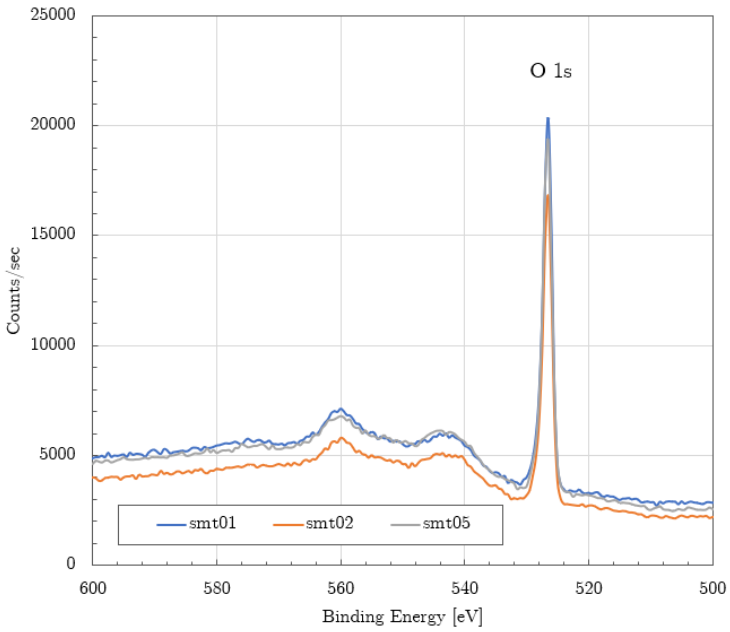

Figure 4.4: Comparison of oxygen peaks in XPS spectra for several grown $SmTiO_3$ films.

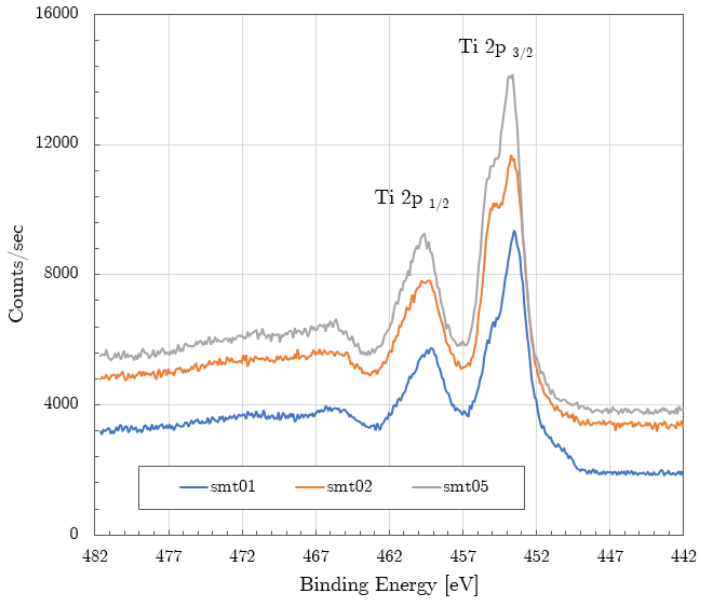

Figure 4.5: Comparison of titanium peaks in XPS spectra for several grown $SmTiO_3$ films.

5 CONCLUSION AND FURTHER WORK

5.1 Conclusion

5.1.1 $NdNiO_3$ Soft X-ray Spectroscopy and Magnetic Scattering

In this work we present characterization of the electronic and magnetic properties of a novel freestanding $NdNiO_3$ thin film. In our XAS results, we find that the metal insulator transition occurs over the anticipated temperature range (100 K to 180 K). The metal-insulator transition temperature is noted to be 145 K on cooling and 150 K on heating, showing a small hysteresis with a width, $\Delta T_{MI} = 5$ K. Through x-ray magnetic scattering, we find that the transition between antiferromagnetic and paramagnetic phases occurs concurrently with the electronic transition (130 K to 150 K) as expected in $NdNiO_3$. As this experiment was conducted only on heating, we do not have insight into any hysteresis in the magnetic transition.

STXM stacks were collected across the electronic transition temperature range, with results in agreement with the XAS. Defect domains were observed in this sample which displayed no temperature dependent spectral changes (no metal insulator transition). No distinct metallic and insulating phase domains were observed.

Our STXM imaging resolution and scale would have been suitable to observe features on the order of those reported in recent studies and our temperature range and step size were appropriate to capture both predominantly metallic and predominantly insulating states. As we did not observe distinct metallic or insulating domains, we suspect that the presence of such domains was either obscured by the periodic noise present in the STXM stacks or by an averaging effect caused by multiple domains forming through the full depth of the sample as illustrated in Figure 3.16. It is also possible that the quality of our films differs from those used in previous studies and the amount and type of defects impacts the formation of

domains.

We hope that the development of growth techniques to fabricate freestanding films of the type examined here coupled with the robust characterization we present of their electronic and magnetic properties compared with those of bulk films presents a step forward in the expansion of possible device architectures. It is contributions of this nature which enable the continuing advances in computing predicted by Moore's law.

5.1.2 $SmTiO_3$ Molecular Beam Epitaxy

Optimizing MBE growth of $SmTiO_3$ thin films at REIXS SSF would enable future study of heterostructures and interfaces displaying tunable electronic properties as well as more exotic emergent properties. Here, we lay the foundations for this work. In this study, $SmTiO_3$ films were successfully grown with the desired layer periodicity and approximate composition, though the XPS Ti 2p peak shapes may indicate some oxygen deficiency. Encouragingly, no impurities were found in analysis of the XPS results. There is room for improvement, however, as growth tended toward the formation of islands rather than uniform deposition across the substrate area.

5.2 Further Work

5.2.1 $NdNiO_3$ Freestanding Films

The initial XAS study was conducted from 100 K to 300 K on the assumption that this would encompass the entire electronic phase transition, but as we see these results, the insulating phase does not saturate within this range. This is further confirmed by the x-ray magnetic scattering results wherein we see that the magnetic phase transition is still in progress down to 80 K. Although these results taken together give a reasonable picture of the two concurrent transitions, it would be beneficial to collect XAS to a lower temperature, perhaps as far as 30 K to ensure that the most insulating state has been observed. Doing so would permit more accurate fractional fitting results.

A key challenge in analyzing the spectra in the STXM data has been the lack of direct

beam data. Conducting a similar study with a sample which would permit direct beam data to be recorded with each stack would allow for better results both in fractional fitting to the continuous region XAS and the SVD mapping. Of interest also, would be examining a thinner $NdNiO_3$ sample (10-20 nm) to avoid averaging multiple domains through the sample depth.

5.2.2 $SmTiO_3$ Growth

These initial $SmTiO_3$ growth runs present a strong foundation for future work by establishing that films of this type can be grown at the REIXS SSF and by identifying approximate growth parameters. Next steps will center around the optimization of these growth parameters. Due to instrument limits, higher substrate temperatures cannot be investigated, but there are still a few avenues of inquiry in improving film quality. During these growth experiments, there were problems with the samarium effusion cell stability. Fixing this issue could yield higher quality films. Improvements in film morphology were noted at higher oxygen partial pressures, so additional work would likely involve increasing oxygen partial pressure during growth.

Bibliography

[1] Gordon E. Moore. Cramming more components onto integrated circuits, Reprinted from Electronics, volume 38, number 8, April 19, 1965, pp.114 ff. *IEEE Solid-State Circuits Society Newsletter*, 11(3):33–35, September 2006.

[2] Kevin Morris. No More Nanometers. https://www.eejournal.com/article/no-more-nanometers/, July 2020.

[3] John Culver. The CPU Shack Museum. www.cpushack.com.

[4] CPUs by Manufacturer. www.cpu-collection.de.

[5] Intel. Microprocessor Quick Reference Guide. www.intel.com/pressroom/kits/quickreffam.htm#i486.

[6] Gennadiy Shvets. Microprocessors/Central Processing Units (CPUs). www.cpu-world.com.

[7] G. Catalan, R. M. Bowman, and J. M. Gregg. Metal-insulator transitions in $NdNiO_3$ thin films. *Phys. Rev. B*, 62(12):7892–7900, September 2000.

[8] Daniele Preziosi, Laura Lopez-Mir, Xiaoyan Li, Tom Cornelissen, Jin Hong Lee, Felix Trier, Karim Bouzehouane, Sergio Valencia, Alexandre Gloter, Agnès Barthélémy, and Manuel Bibes. Direct Mapping of Phase Separation across the Metal–Insulator Transition of $NdNiO_3$. *Nano Lett.*, 18(4):2226–2232, April 2018.

[9] G. Mattoni, P. Zubko, F. Maccherozzi, A. J. H. van der Torren, D. B. Boltje, M. Hadjimichael, N. Manca, S. Catalano, M. Gibert, Y. Liu, J. Aarts, J.-M. Triscone, S. S. Dhesi, and A. D. Caviglia. Striped nanoscale phase separation at the metal–insulator transition of heteroepitaxial nickelates. *Nature Communications*, 7(1):13141, November 2016.

[10] K. W. Post, A. S. McLeod, M. Hepting, M. Bluschke, Yifan Wang, G. Cristiani, G. Logvenov, A. Charnukha, G. X. Ni, Padma Radhakrishnan, M. Minola, A. Pasupathy, A. V. Boris, E. Benckiser, K. A. Dahmen, E. W. Carlson, B. Keimer, and D. N. Basov. Coexisting first- and second-order electronic phase transitions in a correlated oxide. *Nature Physics*, 14(10):1056–1061, October 2018.

[11] Frithjof Nolting. X-ray Microscopy. In *Paul Scherrer Institute Master School*, Villigen, Switzerland, 2017.

[12] Kaveh Ahadi and Susanne Stemmer. Novel Metal-Insulator Transition at the $SmTiO_3/SrTiO_3$ Interface. *Phys. Rev. Lett.*, 118(23):236803, June 2017.

[13] Clayton A. Jackson, Jack Y. Zhang, Christopher R. Freeze, and Susanne Stemmer. Quantum critical behaviour in confined $SrTiO_3$ quantum wells embedded in antiferromagnetic $SmTiO_3$. *Nature Communications*, 5(1):4258, July 2014.

[14] David Attwood. *Soft X-Rays and Extreme Ultraviolet Radiation: Principles and Applications*. Cambridge University Press, Cambridge, 1999.

[15] Antara Basu-Zych. What are the Energy Range Definitions for EM Radiation? https://heasarc.gsfc.nasa.gov/docs/heasarc/headates/spectrum.html.

[16] K. V. Kaznatcheev, Ch. Karunakaran, U. D. Lanke, S. G. Urquhart, M. Obst, and A. P. Hitchcock. Soft X-ray spectromicroscopy beamline at the CLS: Commissioning results. *Nuclear Instruments and Methods in Physics Research Section A: Accelerators, Spectrometers, Detectors and Associated Equipment*, 582(1):96–99, November 2007.

[17] A. F. G. Leontowich, R. Berg, C. N. Regier, D. M. Taylor, J. Wang, D. Beauregard, J. Geilhufe, J. Swirsky, J. Wu, C. Karunakaran, A. P. Hitchcock, and S. G. Urquhart. Cryo scanning transmission x-ray microscope optimized for spectrotomography. *Review of Scientific Instruments*, 89(9):093704, September 2018.

[18] G. Cressey, C. M. B. Henderson, and G. van der Laan. Use of L-edge X-ray absorption spectroscopy to characterize multiple valence states of 3d transition metals; a new probe

for mineralogical and geochemical research. *Phys Chem Minerals*, 20(2):111–119, July 1993.

[19] Weiwei Gu, Hongxin Wang, and Kun Wang. Nickel L-edge and K-edge X-ray absorption spectroscopy of non-innocent $Ni[S_2C_2(CF_3)_2]_{2n}$ series (n = -2, -1, 0): Direct probe of nickel fractional oxidation state changes. *Dalton Trans.*, 43(17):6406–6413, April 2014.

[20] J. van Elp, G. Peng, B. G. Searle, S. Mitra-Kirtley, Y. H. Huang, M. K. Johnson, Z. H. Zhou, M. W. W. Adams, M. J. Maroney, and S. P. Cramer. Electronic Structure and Symmetry in Nickel L Edge X-ray Absorption Spectroscopy: Application to a Nickel Protein. *J. Am. Chem. Soc.*, 116(5):1918–1923, March 1994.

[21] Frank de Groot. Multiplet effects in X-ray spectroscopy. *Coordination Chemistry Reviews*, 249(1-2):31–63, January 2005.

[22] R. J. Green, M. W. Haverkort, and G. A. Sawatzky. Bond disproportionation and dynamical charge fluctuations in the perovskite rare-earth nickelates. *Phys. Rev. B*, 94(19):195127, November 2016.

[23] OpenStax. *Chemistry*. OpenStax, June 2016.

[24] Masatoshi Imada, Atsushi Fujimori, and Yoshinori Tokura. Metal-insulator transitions. *Rev. Mod. Phys.*, 70(4):1039–1263, October 1998.

[25] G. Koster, M. Huijben, and G. Rijnders. *Epitaxial Growth of Complex Metal Oxides*. Number 76 in Woodhead Publishing Series in Electronic and Optical Materials. Elsevier, 2015.

[26] M. Hepting, R. J. Green, Z. Zhong, M. Bluschke, Y. E. Suyolcu, S. Macke, A. Frano, S. Catalano, M. Gibert, R. Sutarto, F. He, G. Cristiani, G. Logvenov, Y. Wang, P. A. van Aken, P. Hansmann, M. Le Tacon, J.-M. Triscone, G. A. Sawatzky, B. Keimer, and E. Benckiser. Complex magnetic order in nickelate slabs. *Nature Phys*, 14(11):1097–1102, November 2018.

[27] Valentina Bisogni, Sara Catalano, Robert J. Green, Marta Gibert, Raoul Scherwitzl, Yaobo Huang, Vladimir N. Strocov, Pavlo Zubko, Shadi Balandeh, Jean-Marc Triscone, George Sawatzky, and Thorsten Schmitt. Ground-state oxygen holes and the metal–insulator transition in the negative charge-transfer rare-earth nickelates. *Nat Commun*, 7(1):1–8, October 2016.

[28] M.A. Herman, W. Richter, and H. Sitter. *Epitaxy: Physical Principles and Technical Implementation*. Springer-Verlag, 2004.

[29] Thomas P. Pearsall, editor. *Strained-Layer Superlattices: Materials Science and Technology*, volume 33 of *Semiconductors and Semimetals*. Elsevier, 1990.

[30] Sang Hyo Kweon, Jong-Hyun Kim, Mir Im, Woong Hee Lee, and Sahn Nahm. Physical Properties of $(Na_{1-x}K_x)NbO_3$ Thin Film Grown at Low Temperature Using Two-Dimensional $Ca_2Nb_3O_{10}$ Nanosheet Seed Layer. *ACS Appl. Mater. Interfaces*, 10(30):25536–25546, August 2018.

[31] Huiyu Yuan, Roy Lubbers, Rogier Besselink, Maarten Nijland, and Johan E. ten Elshof. Improved Langmuir–Blodgett Titanate Films via in Situ Exfoliation Study and Optimization of Deposition Parameters. *ACS Appl. Mater. Interfaces*, 6(11):8567–8574, June 2014.

[32] Huiyu Yuan, Minh Nguyen, Tom Hammer, Gertjan Koster, Guus Rijnders, and Johan E. ten Elshof. Synthesis of $KCa_2Nb_3O_{10}$ Crystals with Varying Grain Sizes and Their Nanosheet Monolayer Films As Seed Layers for PiezoMEMS Applications. *ACS Appl. Mater. Interfaces*, 7(49):27473–27478, December 2015.

[33] Shuji Hasegawa and Elton N. Kaufmann. Reflection High-Energy Electron Diffraction. In *Characterization of Materials*, page 14. John Wiley & Sons, Inc., 2012.

[34] Jin Hong Lee, Felix Trier, Tom Cornelissen, Daniele Preziosi, Karim Bouzehouane, Stéphane Fusil, Sergio Valencia, and Manuel Bibes. Imaging and Harnessing Percolation at the Metal–Insulator Transition of $NdNiO_3$ Nanogaps. *Nano Lett.*, 19(11):7801–7805, November 2019.

[35] Huiyu Yuan, David Dubbink, Rogier Besselink, and Johan E. ten Elshof. The Rapid Exfoliation and Subsequent Restacking of Layered Titanates Driven by an Acid-Base Reaction. *Angew. Chem. Int. Ed.*, 54(32):9239–9243, August 2015.

[36] Linfeng Hu, Min Chen, Xiaosheng Fang, and Limin Wu. Oil–water interfacial self-assembly: A novel strategy for nanofilm and nanodevice fabrication. *Chem. Soc. Rev.*, 41(3):1350–1362, 2012.

[37] Phu T.P. Le, Johan E. ten Elshof, and Gertjan Koster. Shape Control of Ca $_2$ Nb $_3$ O $_{10}$ Nanosheets: Paving the Way for Monolithic Integration of Functional Oxides with CMOS. *ACS Appl. Nano Mater.*, 3(9):9487–9493, September 2020.

[38] María Luisa Medarde. Structural, magnetic and electronic properties of perovskites (R = rare earth). *J. Phys.: Condens. Matter*, 9(8):1679–1707, February 1997.

[39] V. Scagnoli, U. Staub, A. M. Mulders, M. Janousch, G. I. Meijer, G. Hammerl, J. M. Tonnerre, and N. Stojic. Role of magnetic and orbital ordering at the metal-insulator transition in $NdNiO_3$. *Phys. Rev. B*, 73(10):100409, March 2006.

[40] David Nečas and Petr Klapetek. Gwyddion: An open-source software for SPM data analysis. *Open Physics*, 10(1):181–188, February 2012.

[41] John F. Moulder, William F. Stickle, Peter E. Sobol, and Kenneth D. Bomben. *Handbook of X-ray Photoelectron Spectroscopy*. Perkin-Elmer Corps. Physical Electronics Division, Eden Prairie, MN, USA, second edition, 1992.

[42] R. S. Ajimsha, M. P. Joshi, S. Raj Mohan, Amit. K. Das, P. Misra, L. M. Kukreja, and D. M. Phase. Band offset at TiO $_2$ /MDMO PPV and TiO $_2$ /PEDOT PSS interfaces studied using photoelectron spectroscopy. *RSC Adv.*, 5(118):97891–97897, 2015.

[43] G. Drera, G. Salvinelli, A. Brinkman, M. Huijben, G. Koster, H. Hilgenkamp, G. Rijnders, D. Visentin, and L. Sangaletti. Band offsets and density of Ti3+ states probed by X-ray photoemission on $LaAlO_3/SrTiO_3$ heterointerfaces and their $LaAlO_3$ and $SrTiO_3$ bulk precursors. *Phys. Rev. B*, 87(7):075435, February 2013. Comment: Submitted to Physical Review B, revised version.

[44] Mark C. Biesinger, Leo W. M. Lau, Andrea R. Gerson, and Roger St. C. Smart. Resolving surface chemical states in XPS analysis of first row transition metals, oxides and hydroxides: Sc, Ti, V, Cu and Zn. *Applied Surface Science*, 257(3):887–898, November 2010.